Estimating particle size and coercivity distributions of pigmentary hematite in red chert with thermal fluctuation tomography

Pengxiang Hu[1,2], Xiang Zhao[1,2], David Heslop[1,2], Hirokuni Oda[2], Andrew P. Roberts[1,2]

[1] *Research School of Earth Sciences, Australian National University, Canberra, ACT 2601, Australia*

[2] *Research Institute of Geology and Geoinformation, Geological Survey of Japan, National Institute of Advanced Industrial Science and Technology (AIST), AIST Tsukuba Central 7, 1-1-1 Higashi, Tsukuba, Ibaraki, 305-8567, Japan*

Corresponding author: Pengxiang Hu (pengxiang.hu@anu.edu.au)

Key Points:

- Thermal fluctuation tomography is applied to red cherts to estimate grain size and microcoercivity distributions of pigmentary hematite
- Fine hematite particles (35 - 160 nm) occur in all samples including superparamagnetic hematite down to a few nanometers
- Temperature-dependent coercivity variations in pigmentary hematite follow Kneller's law

Plain language Summary

Pigmentary hematite widely presents in rocks and sediment and is crucial for paleomagnetic and paleoenvironmental studies because they can record ancient earth magnetic field and past climate signals. As the most important properties in paleomagnetic and paleoenvironmental applications, the coercivity and grain size distribution of natural pigmentary hematite is poorly constrained due to the weak magnetism of hematite and the small size. In this study, we provide a strategy using low-temperature demagnetization curves for estimating joint particle volume and microcoercivity distribution of pigmentary hematite in Inuyama red chert samples. The hematite coercivity increases exponentially with decreasing temperature. Hematite microcoercivity without thermal fluctuation has a wide but approximately symmetric distribution in logarithmic

space from ~1 tesla to tens of tesla. The grain size of hematite varies from several nanometers to about 160 nm. The fine particle size of these hematite results in low unblocking temperature, which makes them suitable to record remagnetization in geological time.

Abstract

Pigmentary hematite carries important signals in paleomagnetic and paleoenvironmental studies. However, weak magnetism and the assumption that it has high magnetic coercivity prevents routine identification of the size distribution of pigmentary hematite, especially for fine particle sizes. We present a strategy for estimating joint hematite particle volume and microcoercivity (f (V, H_{k0})) distributions from low-temperature demagnetization curves and thermal fluctuation tomography (TFT) of pigmentary hematite in bulk samples of Triassic-Jurassic Inuyama red chert, Japan. The coercivity of the pigmentary hematite increases exponentially with decreasing temperature, following a modified Kneller's law, where microcoercivity has a wide but approximately symmetric distribution in logarithmic space from ~1 tesla to tens of tesla. All of the red chert samples contain stable single domain (SSD) hematite with 35 - 160 nm diameter; a significant superparamagnetic (SP) hematite population with sizes down to several nanometers also occurs in Jurassic samples. The SP/SSD threshold size is estimated to be 8 - 18 nm in these samples. The fine particle size of the pigmentary hematite is evident in its low median unblocking temperature (194 °C to 529 °C) and, thus, this hematite may contribute to all four paleomagnetic components identified in published thermal magnetization studies of the Inuyama red chert. In this work, uniaxial anisotropy and magnetization switching via coherent rotation are assumed. Uniaxial anisotropy is often dominant in fine-grained hematite, although the dominant anisotropy type should be evaluated before using TFT. This approach is applicable to studies that require knowledge of coercivity and size distributions of hematite pigments.

1. Introduction

Hematite is abundant in sedimentary rocks, especially red beds. It occurs commonly as a fine-grained chemically precipitated pigment and as coarser detrital or specular hematite (Cornell and Schwertmann, 2003; Lepre and Olsen, 2021; Jiang et al., 2022; Swanson-Hysell et al., 2019; Tauxe

et al., 1980). Poorly crystalline pigmentary hematite can be the dominant iron oxide in many red soils and sediments and is responsible for their characteristic red color. Both specular and pigmentary hematite can carry magnetic remanence. Specular hematite carries a detrital remanent magnetization (DRM), which is often assumed to be a primary or near-primary magnetization. Widely observed red bed remagnetizations tend to be associated with late diagenetic pigmentary hematite formation. Debate about whether red beds record a primary DRM or a secondary chemical remanent magnetization (CRM) led to the "red bed controversy" (Beck et al., 2003; Butler, 1992; Van Der Voo & Torsvik, 2012). Identification of CRM acquisition in pigmentary hematite can enable more accurate paleomagnetic interpretations in regional tectonic studies (Abrajevitch et al., 2018; Jiang et al., 2017; Swanson-Hysell et al., 2019). As the most abundant surficial iron oxide on Earth resulting from near-surface processes, hematite is also an excellent recorder of paleoenvironmental signals. Its formation via authigenic chemical processes means that pigmentary hematite is used as an indicator of hydration conditions, acidity of aqueous environments, and monsoon evolution (e.g., Larrasoaña et al., 2003; Abrajevitch et al., 2013; Lepre and Olsen, 2021). Despite the usefulness of pigmentary hematite as a paleoclimatic indicator or as a carrier of paleomagnetic records, it is often described vaguely as a "fine hematite population", with poorly constrained coercivity and grain size distributions.

Characterizing the grain size and coercivity of pigmentary hematite is challenging because it is necessary to overcome the combined difficulty of detecting weakly magnetic hematite when it co-occurs with other magnetic minerals and characterizing poorly crystalline nanoparticles. Magnetite has a spontaneous magnetization that is more than 200 times stronger than hematite, so even small amounts of magnetite can overwhelm the magnetic contribution of hematite (Dekkers, 1990; Frank and Nowaczyk, 2008; Roberts et al., 2020). In practice, hematite detection in natural samples often relies on its high coercivity and distinctive color (Roberts et al., 2020; Jiang et al., 2022 and references therein). However, the small size and often poorly crystalline nature of hematite nanoparticles means that hematite concentrations can be difficult to determine with many spectroscopic approaches. Such particles will also be responsible for a substantial low-coercivity distribution that is not usually attributed to hematite in mineral magnetic studies, especially when using magnetic parameters with cut-off fields of 300 mT (Roberts et al., 2020). Isothermal remanent magnetization (IRM) component analysis appears to be the most suitable magnetic

method for detecting hematite because it enables estimation of continuous, non-truncated coercivity distributions (Hu et al., 2021; Roberts et al., 2020). However, superparamagnetic (SP) pigmentary hematite, which is abundant in natural environments (Collinson, 1969; Schwertmann, 1991), will not be evident in room temperature IRM results. Color and diffuse reflectance methods also have limitations for detecting or quantifying hematite because they depend strongly on grain size and crystallinity. Decreasing grain size tends to reduce the reflectance wavelength and changes the color from purple-red to yellow-red (Cornell and Schwertmann, 2003; Jiang et al., 2022). Evaluating grain size distributions for pigmentary hematite is, therefore, difficult because grain size influences most proxies used to estimate hematite properties.

Microscopy observations reveal the existence of nano-sized hematite with sizes from ~20 nm to a few hundred nanometers in soils and banded iron formations (Egglseder et al., 2018; Hyodo et al., 2020; Sun et al., 2015). A more systematic relationship between hematite grain size and unblocking temperature has been established by Swanson-Hysell et al. (2011, 2019) using Néel (1949) relaxation theory. The grain size range of remanence-carrying hematite can be inferred using unblocking temperatures from thermal demagnetization experiments, although this approach cannot be used to estimate SP particles because they do not carry a stable remanence at room temperature.

Grain volume is a key variable in Néel (1949) theory. Dunlop (1965) pointed out that it is possible to combine field- and temperature-dependent measurements to determine the joint grain volume (V) and microcoercivity at absolute zero (H_{k0}) distribution; f (V, H_{k0}). Jackson et al. (2006) developed a procedure to estimate f (V, H_{k0}) for particle assemblages that contain both SP and stable single domain (SSD) magnetite based on backfield remanence curves measured over a range of temperatures, which they called “thermal fluctuation tomography” (TFT). This method was used to reconstruct the grain size distribution of magnetite in both synthetic and natural tuff and paleosol samples. Theoretically, TFT can also be used for weakly magnetic minerals like hematite that have a wider size range for SSD behaviour (Banerjee, 1971; Kletetschka and Wasilewski, 2002; Özdemir and Dunlop, 2014). Here, we present a TFT procedure to estimate the grain size and microcoercivity distribution for pigmentary hematite in natural red chert samples based on the approach of Jackson et al. (2006). Multiple low-temperature magnetic measurements are integrated

to constrain the magnetic mineralogy of natural hematite-magnetite-bearing samples. Our results also provide new insights into the nature of pigmentary hematite in red sedimentary rocks.

2. Materials and Methods

2.1. Inuyama red chert

Red chert is a distinctive hematite-rich biosiliceous sedimentary rock, which was a common pelagic marine sediment type from the Ordovician to the early Late Cretaceous (Jones and Murchey, 1986). The Inuyama red chert crops out along the Kiso River about 30 km north of Nagoya, Japan. Red chert, gray chert, and siliceous claystone were deposited alternately over thicknesses of several hundred meters in the middle Triassic to early Jurassic (Oda and Suzuki, 2000). Hematite occurs as a finely dispersed pigment of chemical origin in red cherts (Jones and Murchey, 1986; Matsuo et al., 2003). The Inuyama red chert contains variable mixtures of magnetite and pigmentary hematite (Oda and Suzuki, 2000; Abrajevitch et al., 2011; Hu et al., 2021). Four representative samples were selected from three red bedded chert sites (KA1, KA6, UN2) in the Inuyama area. Biostratigraphic, paleomagnetic, and rock magnetic results for the same sample set have been published by Oda and Suzuki (2000) and Hu et al. (2021). Radiolarian fossils indicate that the KA1 and UN2 samples have middle (Anisian) and late Triassic (Norian) ages while two KA6 samples are of early Jurassic age (Oda and Suzuki, 2000).

2.2. Low temperature magnetic measurements

Samples were cut into 4 mm × 4 mm × 3 mm pieces and were measured with a Quantum Design Magnetic Properties Measurement System (MPMS) at the Black Mountain Paleomagnetism Laboratory, Australian National University. First, an isothermal remanent magnetization (IRM) was imparted at 10 K in a 5 T field (LTSIRM) after cooling in zero field (ZFC) and then demagnetized by ramping the superconducting magnet down in oscillation mode from 100 to 0 mT to simulate an alternating field (AF) demagnetization at 10 K (Lagroix and Guyodo, 2017). The resulting magnetization was then measured from 10 K to 300 K to obtain $LTIRM_{@AF100}$ warming curves. Following the same protocol, $LTIRM_{@AF300}$ warming curves were also measured for the same sample by ramping the magnet down from 300 to 0 mT after imparting a LTSIRM.

In this way, magnetizations carried over different coercivity ranges (>300 mT, 100-300 mT, and <100 mT) were separated to identify their low temperature characteristics. In this study, $LTIRM_{>300\ mT}$ is represented by $LTIRM_{@AF300}$, $LTIRM_{100\text{-}300\ mT}$ is given by $LTIRM_{@AF100}$ - $LTIRM_{@AF300}$, and $LTIRM_{<100\ mT}$ is calculated as LTSIRM - $LTIRM_{@AF100}$. Second, a 5 T field was imparted again at 10 K after ZFC and IRM was measured in zero field during warming to 300 K to obtain ZFC-LTSIRM curves. Samples were then field-cooled (FC) to 10 K in a 5 T field and measured during warming back to 300 K after removing the field (FC-LTSIRM). Third, backfield demagnetization curves were measured for the same four samples at 50 logarithmically spaced steps from 0.001 T to 5 T after being saturated with an initial 5 T field at eight temperatures: 300 K, 250 K, 200 K, 150 K, 100 K, 80 K, 50 K, and 10 K. These curves were later decomposed into skew-normal coercivity components using the fitting software MAX UnMix (Maxbauer et al., 2016). Finally, to test for goethite contributions that will be fully demagnetized at 400 K, samples were given a room temperature IRM (RTSIRM) in a 5 T field and were demagnetized by ramping the magnet from 300 to 0 mT in oscillation mode. The remaining remanence $RTSIRM_{@AF300}$ was measured in zero field during cooling to 150 K and then during warming to 400 K and then during cooling back to 150 K.

3. Thermal fluctuation tomography theory for hematite

We adapted the tomographic imaging method of Jackson et al. (2006) to estimate f (V, H_{k0}) distributions for SP and SDD hematite grains. The procedure is described briefly below, with focus on modifications made for hematite. For a detailed explanation and derivation of TFT theory, see Jackson et al. (2006) and Dunlop (1965).

The TFT approach involves using backfield remanence data to estimate the blocking field (H_B). For hematite at a given temperature, we evaluate $H_B = H_{cr} - H_q$, where H_{cr} is the coercivity of remanence, and H_q is the thermal fluctuation field. For a randomly oriented population of identical grains, H_q is expressed as (equation 8 of Jackson et al. (2006)):

$$H_q = 0.801\left(\frac{kT\sqrt{H_k(T)}}{\mu_0 V M_S(T)}\right)^{\frac{2}{3}} \ln^{\frac{2}{3}}\left[\frac{\tau_{exp}}{\tau_0\mu_0\Delta H_{DC}\sqrt{\mu_0 H_k(T)}} \times \left(\frac{kT}{VM_S(T)}\right)^{\frac{2}{3}}\right], \quad (1)$$

where M_s (T) and H_k (T) are the saturation magnetization and microcoercivity as a function of absolute temperature, T, respectively, μ_0 is the permeability of free space ($4\pi\times10^{-7}$ H/m), k is Boltzmann's constant (1.38×10^{-23} J/K), V is the hematite particle volume, and τ_0 is a characteristic time related to the natural frequency of gyromagnetic precession. For nanosized hematite, τ_0 is found to be 10^{-12} -10^{-11} s (Henrik, 2014 and references therein). We here assume τ_0 10^{-12} s. The exposure time τ_{exp} for the backfield treatments is assigned as 300 s, and ΔH_{DC} is the applied field difference between successive backfields. We assume here that the saturation magnetization at absolute zero (M_{S0}) is 2500 A/m for hematite (Dunlop and Özdemir, 1997), then M_S(T) can be represented using Bloch's 3/2 law (Bloch, 1930):

$$M_S(T) = M_{S0} \times \left(1 - B \times T^{\frac{3}{2}}\right), \quad (2)$$

where B is the Bloch constant. B is determined by the spin-wave stiffness constant; we adopt B = 10^{-5} for hematite nanoparticles (Martínez et al., 1996).

The next step is to describe microcoercivity (H_k) as the function of temperature. Two analytic models have been used previously to describe the temperature dependence of the coercive force.

1. By taking $\frac{H_k(T)}{H_{k0}} = \left(\frac{M_S(T)}{M_{S0}}\right)^n$ (Dunlop and Özdemir, 2000; Jackson et al., 2006; Menyeh and O'Reilly, 1995), where n depends on the dominant anisotropy, we can calculate H_k(T) based on Bloch's 3/2 law:

$$H_k(T) = H_{k0}\left(1 - B \times T^{\frac{3}{2}}\right)^n, \quad (\mathbf{3})$$

   However, hematite anisotropy can be complex and published n values for fine-grained hematite below room temperature are rare. Study of synthetic nano-sized hematite reveals that temperature has a minimal impact on M_S(T) while coercivity increases significantly at low temperature due to frozen canted spins (Satheesh et al., 2017). Therefore, n should be large because of the significant H_k(T) change compared to minimal M_S(T) change. Satheesh et al. (2017) reported M_s and H_c for a 64 nm hematite sample at both 5 K and 300 K, to give a calculated n value of ~10.
2. The temperature dependence of coercivity, H_c (T), can also be expressed by Kneller's law (Kneller and Luborsky, 1963):

$$H_c(T) = H_{c0}\left(1 - \left(\frac{T}{T_B}\right)^{\alpha}\right), \quad (4)$$

where T_B is the blocking temperature for SP particles, α is Kneller's exponent and H_{c0} is the coercivity at absolute zero. For non-interacting single domain nanoparticles with uniaxial anisotropy, α usually takes a value of 0.5 (Kuncser et al., 2020; Maaz et al., 2010; Osman and Moyo, 2015). However, α can deviate from 0.5 due to finite size effects at the nanoscale as well as due to variations in volume distribution, randomness of anisotropy axes, and interparticle interactions (Nayek et al., 2017). Similar to the n value in equation (3), α for hematite nanoparticles is poorly constrained.

To establish a thermally dependent coercivity model for pigmentary hematite in Inuyama red chert, we compare the hematite median H_{cr} values obtained from backfield curve decomposition using both models. First, we need to clarify the relationship among different coercivity forms, H_c, H_{cr} and H_k. Experimental H_{cr}/H_c ratios for SSD hematite are almost constant at ~1.5 (Martin-Hernandez and Guerrero-Suarez, 2012; Peters and Dekkers, 2003; Özdemir and Dunlop, 2014; Roberts et al., 2021). The relationship between H_{cr} and H_k depends largely on the dominant anisotropy type. For randomly oriented identical particles with uniaxial anisotropy, Stoner and Wohlfarth (1948) theory gives $H_{cr}/H_k = 0.524$. Multiaxial anisotropy, such as cubic or hexagonal anisotropy, can increase H_{cr} (Harrison et al., 2019) and therefore raise this ratio close to 1. The high magnetostriction of hematite and weak M_s suggests a high sensitivity to magnetostrictive strain in hematite (Banerjee, 1963); this strain-related anisotropy is taken to be uniaxial. FORC diagrams for the studied red chert samples have "ridge-type" distributions for hematite up to 1.2 T (Hu et al., 2021), which is typical of uniaxial SSD particle assemblages (Egli et al., 2010). Therefore, by assuming a dominant uniaxial anisotropy and relatively constant H_{cr}/H_c ratios for SP/SSD hematite in the Inuyama red chert, we adopt linear relationships among H_c, H_{cr} and H_k. Then, for model 1, we fit the hematite median H_{cr} data using equation (3). Under the assumption of a common n value for all samples, we estimate both H_{cr0} and n using Bayesian regression. Similarly, by assuming a common α value, we fit the hematite H_{cr} data using equation (4) and obtain median posterior estimates of H_{cr0}, T_B, and α via Bayesian regression for model 2 (see section 4.3 for details). By selecting an appropriate model based on our experimental data (section

4.3) and assigning $H_{cr0} = 0.524H_{k0}$, we can estimate $H_k(T)$. Then $H_B(T)$ is obtained by substituting $H_B = 0.524H_k - H_q$ into equation (1).

After constructing field blocking contours for hematite, we describe each hematite grain using two essential attributes, V and H_{k0}. A saturating field applied and removed isothermally at temperature T_1 magnetizes the entire thermally stable population at that temperature (Figure 1, blue shaded region), which corresponds to grains with (V, H_{k0}) that plot above and to the right of the zero-field blocking contour for T_1 (Figure 1). Subsequent application and removal of a reverse DC field, H_1, flips the magnetic moments of grains with (V, H_{k0}) that plot below and to the left of the blocking contour for (T_1, H_1) (Figure 1, hatched area). Each backfield reverses the moments of grains that plot in a region on the Néel diagram (Dunlop, 1965; Néel, 1949) bounded by two blocking field contours for a specified temperature. The change in remanence ΔM_R produced by each DC backfield treatment can, therefore, be expressed as (equation 11 of Jackson et al. (2006)):

$$\Delta M_R = \int f(V, H_{k0}) d\Omega, \text{ and}$$

$$\Omega = \left\{ V, H_{k0} \,\middle|\, H_{i-1} \le H_B \le H_i \right\} \quad (5)$$

where Ω represents the region bounded by two blocking field contours and H_i represents a reverse DC field treatment. Therefore, the procedure is essentially an inverse problem involving $f(V, H_{k0})$ estimation from a series of DC backfield remanence curves for hematite. Details of procedures used to obtain hematite backfield remanence curves are explained in section 4.2.

To estimate $f(V, H_{K0})$, we divided the Néel diagram into a rectilinear grid of cells in which f is uniform in each cell (Figure 1, yellow cell). The discrete equivalent of equation (5) is:

$$\Delta M_{Ri} = \sum_{j=1}^{n_{cells}} f_j a_{ij}, \quad (6)$$

Where a_{ij} is the area of cell j within the area bounded by the blocking contours for a given temperature and applied field used when measuring ΔM_{Ri} (Figure 1, red region). Each temperature and applied field, H_{app}, pair (T, H_{app}) corresponds to a unique blocking contour, defined as the locus of (V, H_{k0}) for which H_B (T, V, H_{k0}) = H_{app}, so we can calculate intersection points of the

contours with the grid lines by piecewise linear interpolation between nodes and approximate the contours by straight-line segments between these intersection points to estimate the areas a_{ij}.

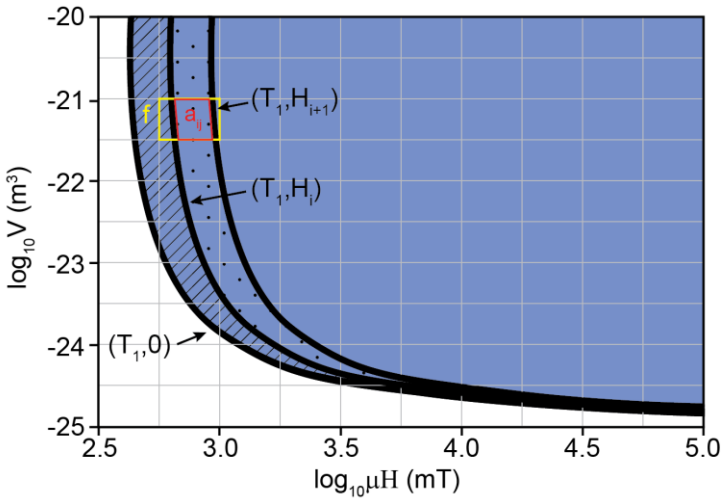

Figure 1 Schematic illustration of the TFT technique, modified from Jackson et al. (2006). A strong field IRM imparted at temperature T_1 is carried by the entire thermally stable population (blue shaded area); a backfield, H_1, applied and removed at temperature T_1, reverses the moments of grains in the hatched area; a larger backfield, H_2, further reverses the moments of grains in the dotted area. a_{ij} (red area) represents the area bounded by the blocking contours for T_1 and applied fields H_{i+1} and H_i when measuring ΔM_{Ri}. The yellow rectangle represents the j^{th} cell, f_j is the value of f (V, H_{k0}) for the j^{th} cell.

We employ an initialization of $f = 0$ at all points to generate a forward model based on equation (6). Residuals are then calculated as the difference between the measured and model remanence data:

$$R_i = \Delta M_{Ri,measured} - \Delta M_{Ri,model} \quad (7)$$

The model is then adjusted by "back-projecting" the residuals:

$$^{s}\Delta f_{ij} = \frac{R_i a_{ij}}{\sum_{k=1}^{n_{cells}} a_{ik}^2}. \quad (8)$$

The adjustment for cell j is proportional to R_i and the area a_{ij} bounded by the blocking contours. n_{cells} represents the number of cells and s represents the current simulation. Stepwise updates are applied after all calculations for each iteration:

$$ {}^{s+1}f_j = {}^{s}f_j + \frac{C}{n_{measurements}} \sum_{i=1}^{n_{measurements}} {}^{s}\Delta f_{ij} (j = 1 \dots n_{cells}) . \quad (9) $$

C is a dimensionless constant used to control the rate of convergence, where higher values cause more rapid convergence, but excessive values can cause the process to become unstable and diverge. Our aim is to reduce the fitting error to ~10% within 100 iterations; after multiple attempts, we found that a C value of 50 generally meets our requirement.

4. Results

4.1. Unblocking of pigmentary hematite

LTSIRM variations of different coercivity fractions for both Triassic and Jurassic red chert samples are shown in Figure 2. The Verwey transition for magnetite is clearly evident at ~120 K for particles with coercivity < 300 mT, which disappears or becomes less noticeable in $LTIRM_{>300}$ curves for the high coercivity component (Figure 2a, 2b), and demonstrating that the coercivity of magnetite is mostly less than 300 mT. For Jurassic specimens, $LTIRM_{>300}$ warming curves decay steeply compared to the relatively flat $LTIRM_{<100}$ curves (Figure 2b), which indicates a wide unblocking temperature distribution of a SP hematite content. A concave shape around 200 K is present in $LTIRM_{>300}$ curves, but not in the low coercivity component, which indicates a likely Morin transition that was not completely smeared out by progressive unblocking of fine hematite (Figure 2b). The $LTIRM_{100\text{-}300}$ warming curve contains both a Verwey transition and marked low temperature unblocking, which suggests a mixture of magnetite and finer hematite in this coercivity range. Hematite unblocking is less significant for Triassic samples, which indicates a smaller SP hematite contribution (Figure 2a). However, $LTIRM_{>300}$ curves for both Triassic and Jurassic samples have comparable magnetizations despite the fact that magnetite has a much stronger magnetization, which indicates that hematite dominates the red chert magnetism by mass.

A Verwey transition is clearly present in both ZFC-LTSIRM and FC-LTSIRM curves, while a Morin transition is likely smeared by progressive unblocking of SP hematite (Figure 2c, 2d). ZFC-LTSIRM and FC-LTSIRM curves are not widely separated, which contrasts with the behavior of

goethite-rich samples (Guyodo et al., 2003; Liu et al., 2006; Huang et al., 2019). Given that the curves almost overlap (Figure 2c, 2d) it is inferred that any goethite contribution is insignificant.

After removing the low coercivity contribution by applying a 300 mT AF, $RTSIRM_{@AF300}$ warming curves decrease gradually from 300 K to 400 K with a net remanence loss during re-cooling (Figure 2e, 2f). No sharp drop is seen at the Néel temperature for goethite. The gradual decrease in warming curves above 300 K is likely due to unblocking of slightly larger hematite particles near the SP/SSD size threshold at room temperature.

4.2. Coercivity distributions for pigmentary hematite

The results shown in Figure 2 indicate that goethite is not magnetically important in the Inuyama red chert and that magnetite is mostly confined to the low coercivity component (< 300 mT). We further examine coercivity spectra at eight temperatures from 10 K to 300 K. At room temperature, most Triassic and Jurassic specimens are well fitted with two skew-normal distributions (Figures 3a, 4a, 4i). One distribution has a 19-35 mT median coercivity and extends from 0 to ~ 500 mT (based on ±3 standard deviations from the median coercivity). The other distribution has a higher median coercivity of 413-598 mT and extends from ~60 mT to ~6 T, which is likely to be due to SSD hematite. Triassic sample UN2-9B-1 has an additional lowest-coercivity contribution with a broad distribution that extends to ~200 mT (Figure 3i). At room temperature there is only a small overlap between the low- and high-coercivity components. With decreasing temperature, the overlap is reduced and finally disappears or becomes insignificant below 100 K. This behavior is consistent with hematite coercivity increasing with decreasing temperature (equations (3) and (4)), while magnetite has a much less dramatic coercivity change with temperature (Özdemir et al., 2002). The low-temperature dividing point of the low-coercivity component appears at ~250 mT, which is consistent with the Verwey transition being significant in the $IRM_{<300}$ component (Figure 2a, 2b). Therefore, for both Triassic and Jurassic specimens, the hematite population can be well separated from magnetite based on their coercivity distributions.

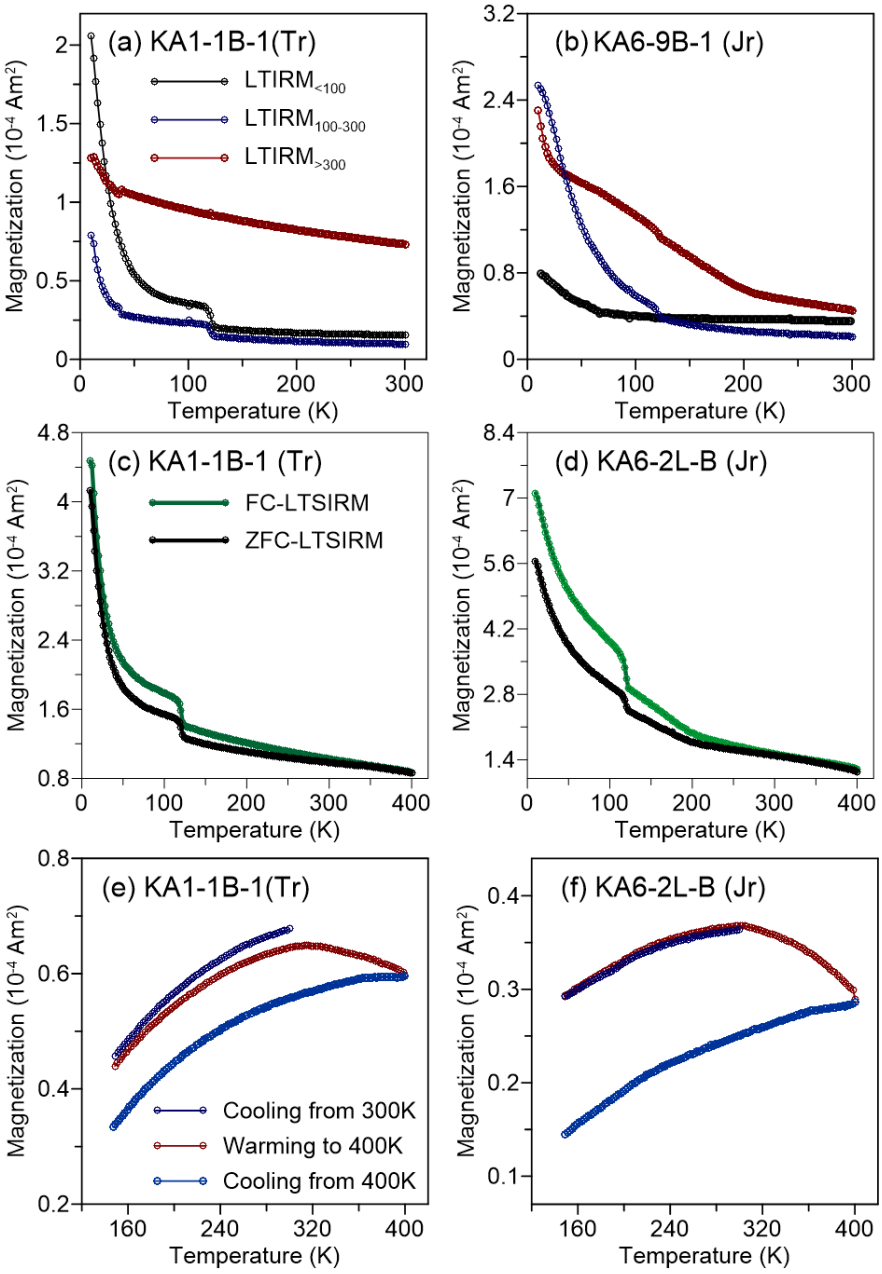

Figure 2 LTSIRM variations versus temperature. (a, b) Samples were given a SIRM in a 5 T field at 10 K and then AF demagnetized in peak fields of 100 and 300 mT, respectively. Then the LTSIRM was measured during warming for components with coercivity ranges of < 100 mT (black), between 100 and 300 mT (blue line), and > 300 mT (red). (c, d) ZFC (black) and FC (green) LTSIRM curves. (e, f) Samples were saturated in a 5 T field at 300 K and then AF demagnetized in a 300 mT peak field. The $RTSIRM_{@AF300}$ was then measured during cooling to 150 K (dark blue), warming to 400 K (red), and then cooling back to 150 K (light blue). Tr = Triassic; Jr = Jurassic.

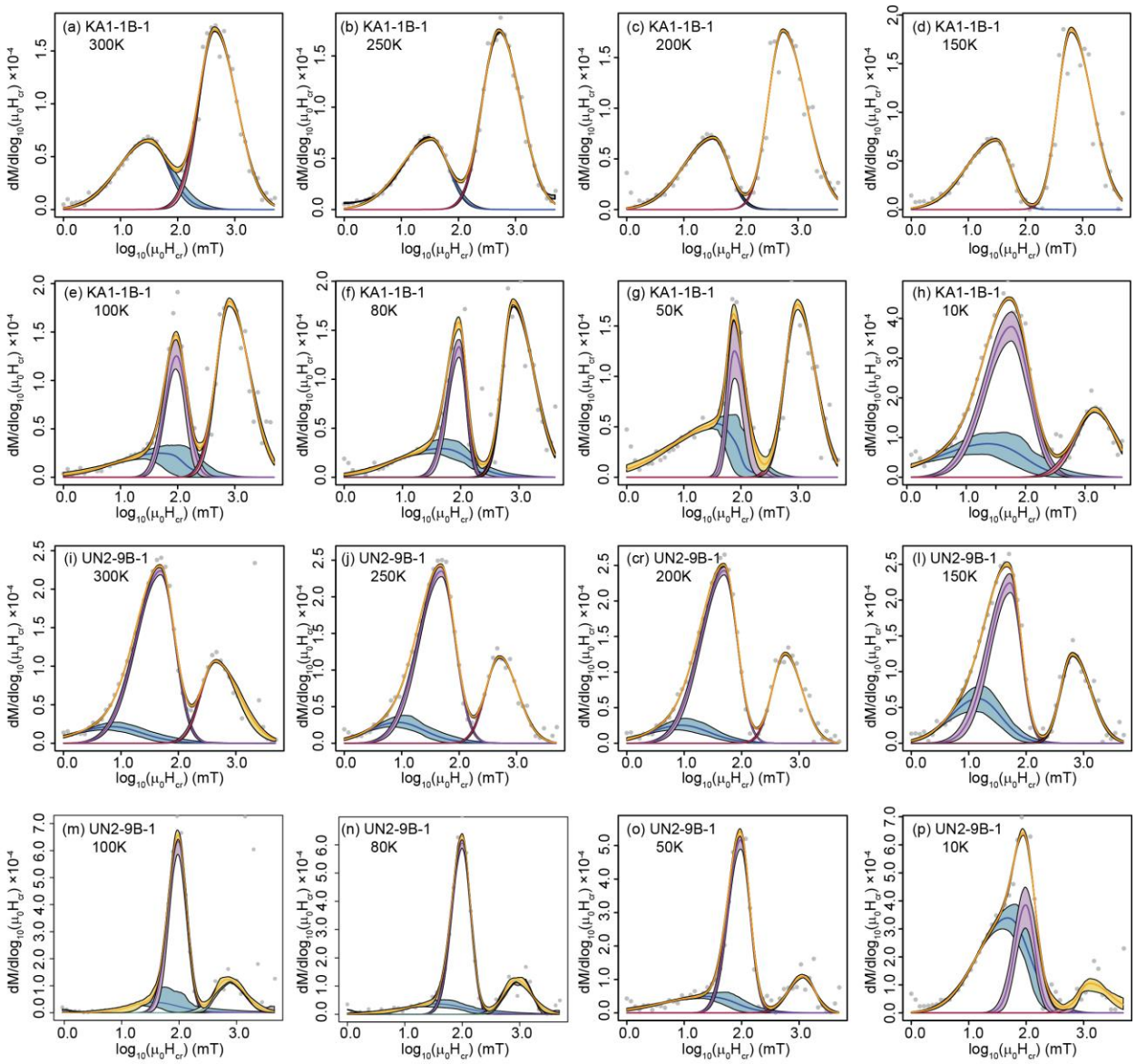

Figure 3 Coercivity spectra from backfield SIRM demagnetization curves for two Triassic specimens (KA1-1B-1, Anisian; UN2-9B-1, upper Norian). The data were fitted using skew-normal distributions with the Max Unmix software (Maxbauer et al., 2016). We fitted data with a minimum number of components. At eight temperatures, the data can be fitted with 2-3 components: the lowest coercivity component is shown in blue, the intermediate coercivity distribution in purple, and the highest coercivity distribution in red. Yellow lines represent the sum of all components, while grey dots represent the data. Shaded areas are 95% confidence intervals for each component.

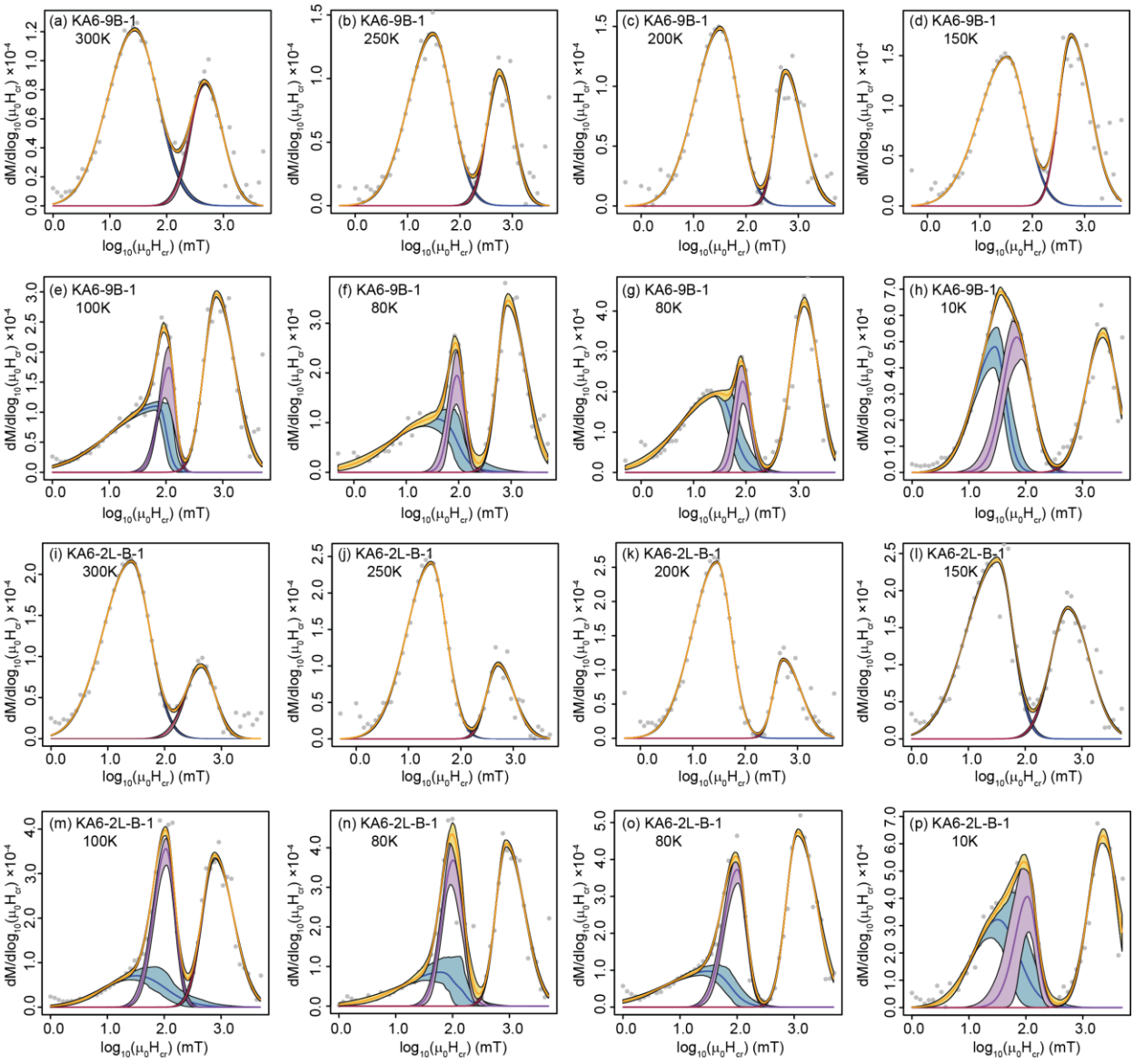

Figure 4 Coercivity spectra from backfield SIRM demagnetization curves for two Jurassic specimens (KA6-9B-1; KA6-2L-B-1 from early Jurassic). Formatting is the same as Figure 3.

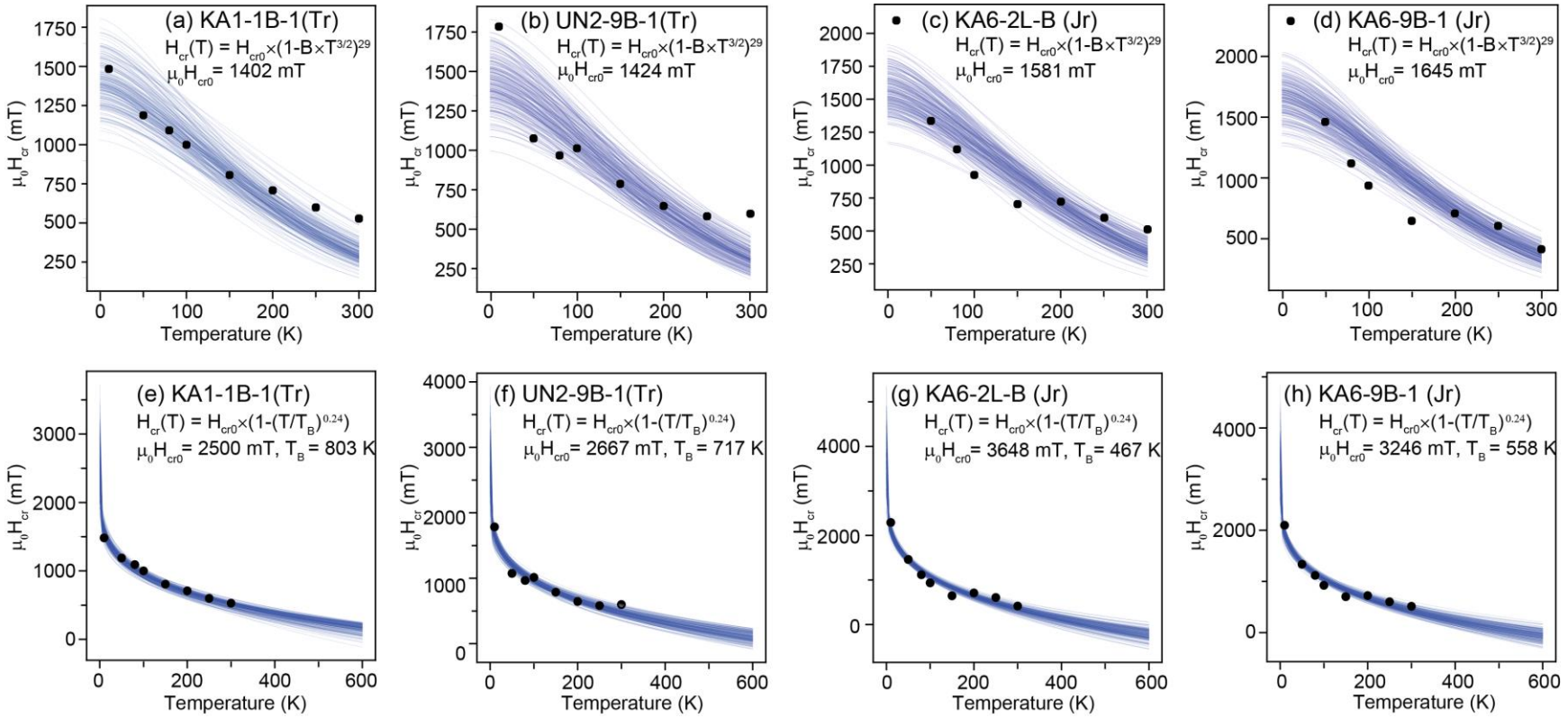

Figure 5 Hematite median remanent coercivity variation with temperature. (a-d) Bayesian posterior distribution of fitted curves based on equation (3) given the priors listed in Appendix A and assuming a common n value for all samples. (e-h) Bayesian posterior distribution of fitted curves based on equation (4) given the Bayesian priors listed in Appendix A and assuming a common value of Kneller's α exponent for all samples. The n and α parameters shown in the equations are the median values from the parameter posterior distributions. Standard deviations and other posterior distribution statistics are provided in Appendix A.

Increases in the coercivity of hematite with decreasing temperature are illustrated in Figure 5. Below ~150 K, the increase is steeper; it triples for Triassic specimens and increases five-fold for Jurassic specimens at 10 K compared to room temperature. The coercivity-temperature fits in Figures 5a-5d and 5e-5h were made using equations (3) and (4), respectively, using Bayesian regression (Appendix A). In this study, we assume that the exponent parameter n or α is constant for pigmentary hematite in Triassic/Jurassic Inuyama red chert. Under this assumption, we combine all 32 data points from four specimens at eight temperatures to estimate a common n and α posterior distribution and individual posterior distributions of H_{cr0} and T_B for each specimen by Bayesian regression (see Appendix A for details). As expected, large n values of 22 - 36 (97% high density interval) are obtained, which demonstrates that the hematite coercivity increases more strongly than M_s. However, these fits are less satisfying at low- and room-temperature. The fits tend to underestimate H_{cr0} and the coercivity close to room temperature due to the flatness of the fitted curves, which largely comes from the 3/2 exponent. Fits based on equation (4) achieve better results (Figure 5e-5h). The posterior α ranges from 0.151 to 0.339 (97% high density interval) with median value of 0.24. Triassic red chert samples have lower H_{cr0} and higher T_B than Jurassic red cherts. Low T_B values of ~ 194 °C and ~ 285 °C are predicted for hematite in Jurassic red cherts, which suggests they have a fine grain size.

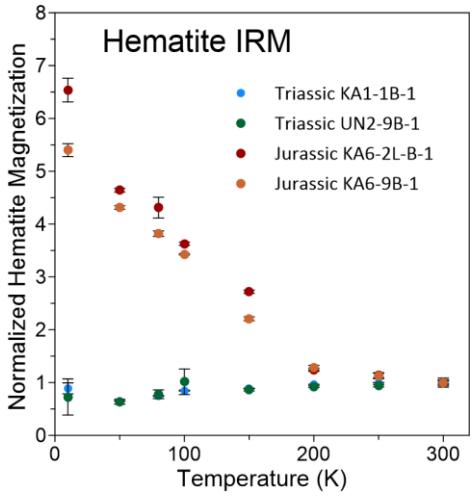

Figure 6 Hematite IRM variation with temperature. Data are normalized by hematite IRM at 300 K for each sample. Error bars represent fitting errors for the hematite component.

Distinctively IRM intensity changes for hematite with temperature are shown for Triassic and Jurassic samples, respectively, in Figure 6. The hematite remanence remains relatively constant for the Triassic specimens (blue and green dots), which indicates that almost all of the hematite is in the SSD state at room temperature. In contrast, hematite remanence increases exponentially with decreasing temperature for the Jurassic samples (brown and red dots), which indicates a significant SP contribution with a wide blocking temperature range.

4.4. Tomographic Analysis

Based on the above results, for our tomographic analysis we adopted Kneller's law as a coercivity-temperature relationship with $\alpha = 0.24$ and $H_{cr} = 0.524H_k$. The median T_B values shown in Figure 5e-5f are used for each specimen to calculate hematite blocking contours. Hematite coercivity distributions extracted from the high-coercivity component fitting in Figures 3 and 4 are shown in Figure 7a-7d. Each dataset contains 808 backfield remanence data points (101 field steps at each of eight temperatures). These data are combined with equations (1) and (4) and are mapped into blocking contours (Figure 7e-7h).

Upon cooling to 10 K, all backfield derivative curves shift progressively to higher coercivities as expected. Peak heights are roughly constant for Triassic samples but increase significantly upon cooling for Jurassic samples (Figure 7). This indicates a greater SP hematite content that blocks gradually with cooling in Jurassic red chert, while the Triassic red chert is dominated by coarser SSD hematite. The blocking contour density is nonuniform, so poor resolution is expected for particles smaller than ~10 nm with microcoercivities less than ~1 T.

After determining the blocking contours, we start the iterative process to calculate the joint grain size and microcoercivity distribution of hematite particles. Best-fit backfield derivative curves reproduce large-scale features of the measured spectra, while still containing higher frequency deviations (Figures A2-A5). Fitting errors are below 15% for all samples.

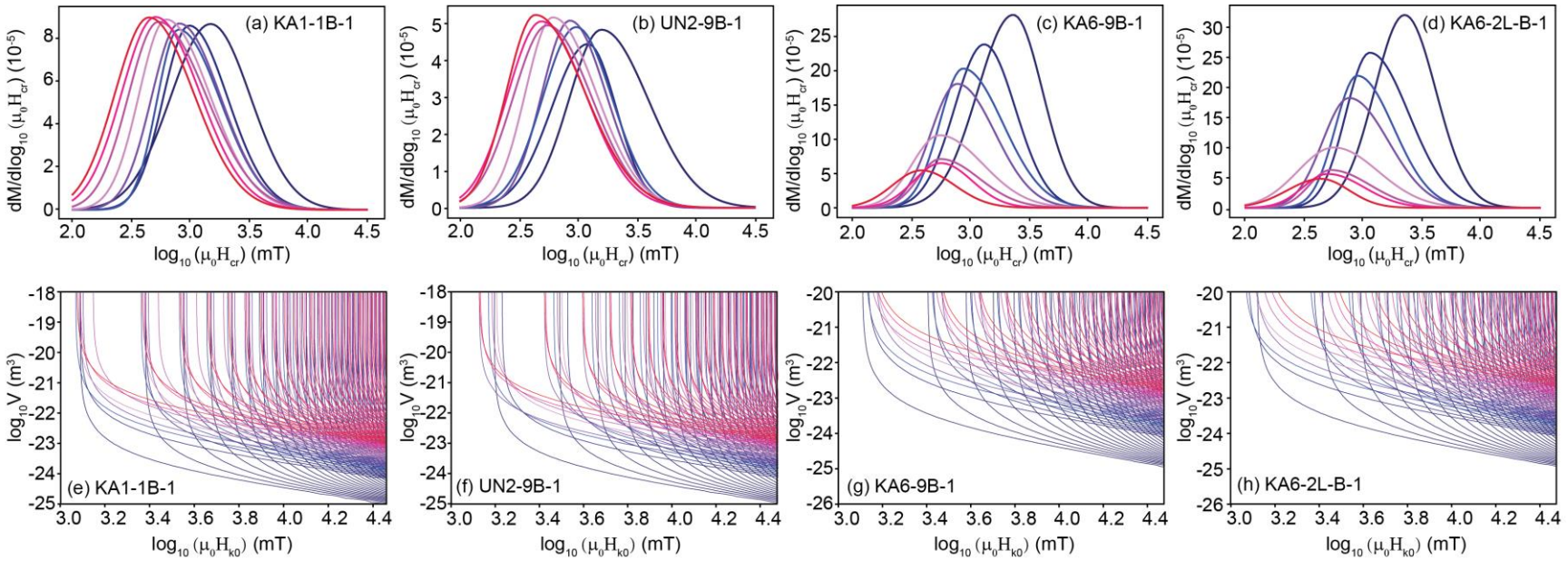

Figure 7 Hematite backfield remanence data and blocking contours for Triassic and Jurassic red cherts. (a-d) Hematite coercivity distributions extracted from backfield LTSIRM decomposition at eight temperatures from 10 K to 300 K. (e-h) Blocking contours for the fields and temperatures in the corresponding datasets above. The equations in Figure 5e-5h are used for each respective specimen. Color variations indicate temperature changes from 10 K (blue) to 300 K (red).

Estimated f (V, H_{k0}) distributions for Triassic samples have a continuous feature centering at volumes around 1×10^{-21} m^3 and microcoercivities between 1 T and 10 T (Figure 8a, 8b). The central volumes are equivalent to spherical hematite particles with ~75 nm diameters. In Jurassic samples, the hematite particles are smaller but magnetically harder (Figure 8c, 8d), with more discrete distributions centered around volumes of ~1×10^{-25} m^3, ~$1\times10^{-23.5}$ m^3, ~$1\times10^{-22.5}$ m^3, and > 1×10^{-22} m^3, which correspond to diameters of ~3 nm, ~11 nm, ~24 nm, and > 35 nm for spherical hematite. The microcoercivity of Jurassic hematite ranges from 3 T to > 30 T. There is clear elongation of the distribution toward the lower right, along with the dominant blocking contour orientation, which may be an artifact of the inversion process (Jackson et al., 2006).

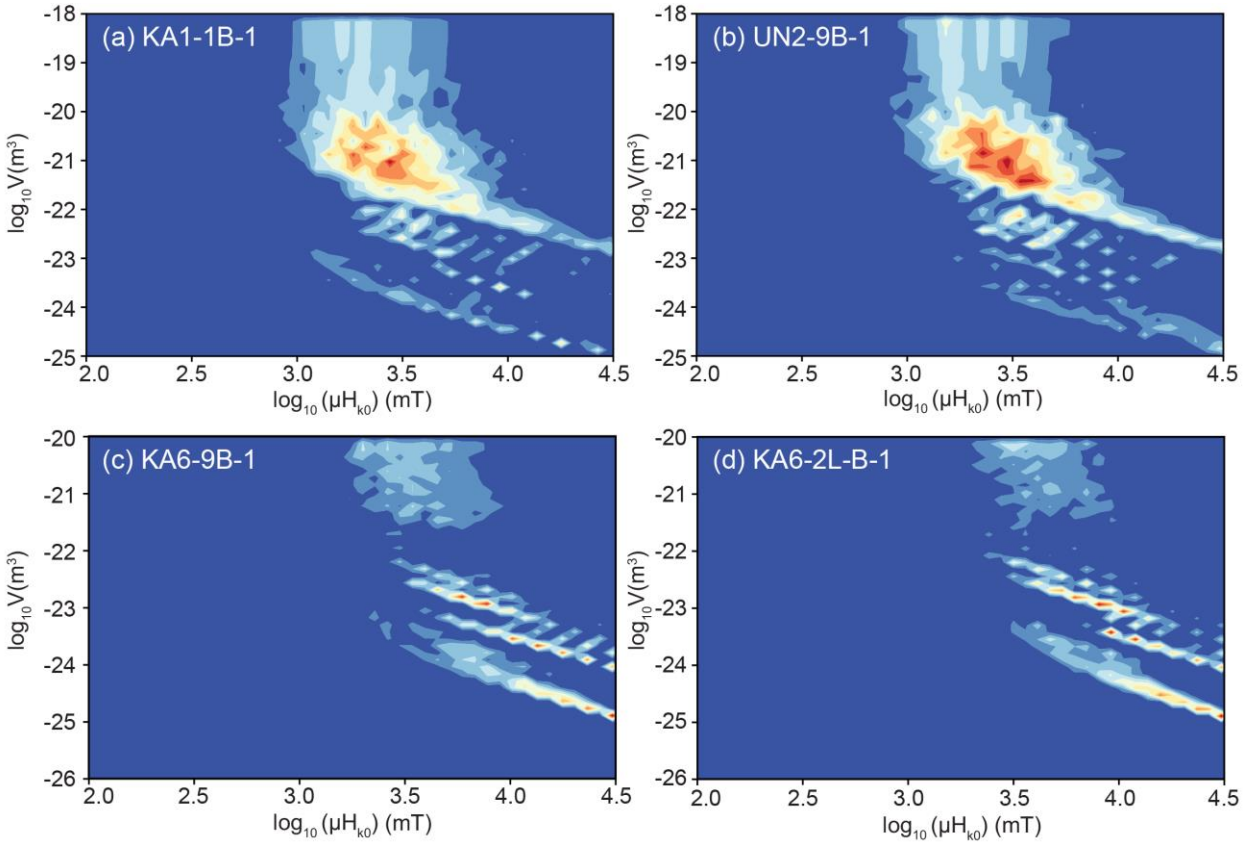

Figure 8 Estimated f (V, H_{k0}) for (a, b) Triassic and (c, d) Jurassic red chert samples from the data in Figure 6a-d. Contour interval = $f_{max}/30$.

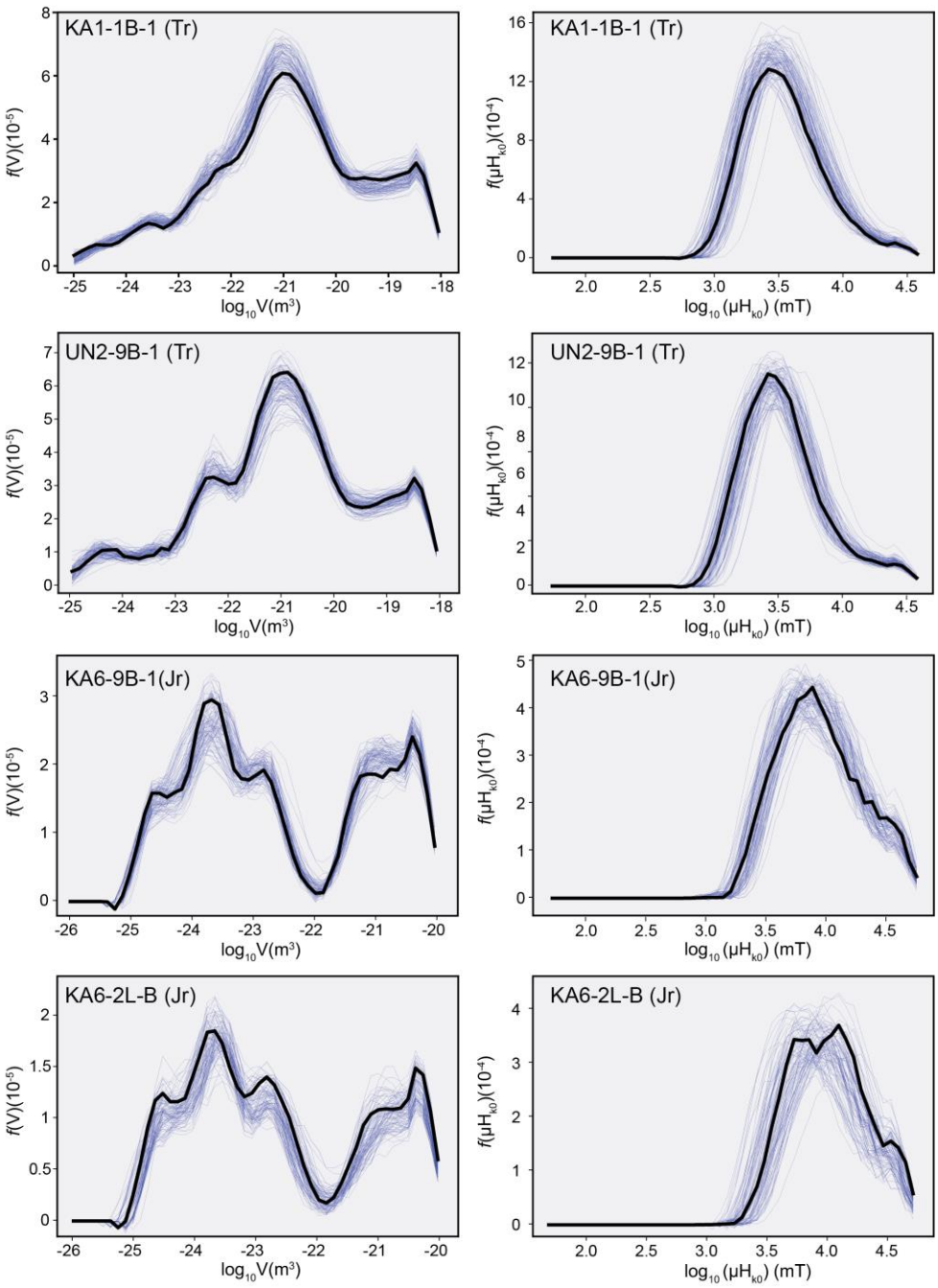

Figure 9 Volume and microcoercivity distributions obtained by summing the rows and columns of the 2D model. The data were smoothed with a Savitzky-Golay filter with window length of 5 in 'nearest' mode using the Python Scipy.signal package. Thick black lines represent the median value; light blue lines represent calculations based on 100 randomly drawn T_B and α values from the Bayesian posterior distribution in Figure A1, which are used to indicate the uncertainty on the calculation of the volume and microcoercivity distribution.

Bayesian modeling was used to calculate the volume and microcoercivity distributions shown in Figure 9. Thick black lines represent the median volume and microcoercivity distribution for each sample based on median T_B and α values. The light blue lines represent calculations based on 100 randomly drawn T_B and α values from their Bayesian posterior distribution in Figure A1, which indicates the uncertainty on the volume and microcoercivity distribution calculation. The marginalized microcoercivities are nearly lognormally distributed. Additional high microcoercivity contributions (> 10 T) are more evident in the Jurassic hematite than Triassic hematite. By contrast, volume distributions are asymmetrical and more complex. Triassic hematite populations have a small peak at 1×10^{-23} to 1×10^{-22} m^3 and then gradually increase to a major peak at ~1×10^{-21} m^3 (Figure 9a). Additional coarse particles with volume larger than 1×10^{-20} m^3 are also present. The Jurassic hematite population has a roughly bimodal distribution separated at around 1×10^{-22} m^3. The larger particle population has a broad peak from 1×10^{-22} m^3 to 1×10^{-20} m^3. The smaller particle population has a major peak at ~1×10^{-24} m^3 with two smaller peaks at $1\times10^{-24.6}$ m^3 and 1×10^{-23} m^3, which correspond to their discrete components in Figure 8c, 8d. The discrete nature of the distribution is most likely due to the limited numbers of temperatures used here because the distributions are all elongated along the unblocking contours. Nevertheless, two grain size populations are evident in Jurassic samples; the finer fraction ranges from a few nanometers to ~35 nm in diameter while the coarser fraction is from ~35 nm to ~160 nm in diameter and is comparable with Triassic samples.

5. Discussion

5.1. Coercivity of pigmentary hematite in red chert

Early studies of the Inuyama red chert reported large saturating fields of up to several tesla for pigmentary hematite from IRM acquisition curves (Oda and Suzuki, 2000; Shibuya and Sasajima, 1986). In our results, room temperature μ_0H_{cr} ranges from ~60 mT to ~6 T in Triassic red chert and from ~70 mT to ~3 T in Jurassic red chert (Figures 3 and 4), which is comparable to recent studies (Abrajevitch et al., 2013; Hu et al., 2021). Published data for pigmentary hematite in red beds have a similarly wide range of μ_0H_{cr} values. In the Deer Lake Group red beds of western Newfoundland, hematite remanent coercivity ranges from ~60 mT to 3 T (Bilardello and Kodama, 2010a), and for red beds from the Maritime provinces of Canada, it varies from ~40 mT to 5 T and

beyond (Bilardello and Kodama, 2010b). Hematite in Triassic red beds from South China has remanent coercivity values from ~60 mT to 3 T (Jiang et al., 2017). For zebra rock in Western Australia, strong fields up to 3 T are needed to saturate hematite (Abrajevitch et al., 2018). North American red siltstone intraclasts have remanent coercivity of ~100 mT to 1.8 T and beyond (Swanson-Hysell et al., 2019). Thus, $\mu_0 H_{cr}$ values of ~60 mT to ~3 T are typical of natural pigmentary hematite in red beds, although values up to even ~6 T are sometimes observed. This $\mu_0 H_{cr}$ range gives an idea of the remanent coercivity distribution of natural SSD pigmentary hematite.

We further illustrate remanent coercivity variations with temperature for pigmentary hematite. H_{cr} increases exponentially with decreasing temperature, following the T^{α} law, where $\alpha = 0.24$ is the median posterior value for red chert samples in this study (Figure 5e, 5f, 5g, 5h). This behavior can be understood by considering thermal fluctuation effects of blocked moments across an anisotropy barrier (Maaz et al., 2010). For natural pigmentary hematite, this simple thermal activation model appears to be applicable from 10 K to 300 K. The significant H_{cr} increase at low temperatures also provides a way to separate a hematite component from magnetite. Based on results in Figures 2 and 3, there is almost no overlap between magnetite and hematite components below 100 K.

Quintupled hematite M_{rs} values at 10 K compared to room temperature confirms the presence of a large SP hematite population in the Jurassic red chert (Figure 6). The steep M_{rs} rise below 200 K indicates that the blocking temperature of most SP hematite is below 200 K. Our results demonstrate that decomposition of low temperature backfield curves reveals and potentially enables quantification of entire pigmentary hematite populations, especially SP particles. Although SP signatures are detected in remanent FORC diagrams (Hu et al., 2021), these signals tend to be dominated by magnetite because FORC diagrams reflect bulk signals and the magnetization of hematite is more than two hundred times lower than magnetite (Dunlop and Özdemir, 1997).

Compared to room-temperature H_{cr}, which only represents SSD populations, H_{k0} provides a measure of the entire hematite population, including SP particles. In the calculations of Jackson et al. (2006), $\mu_0 H_{k0}$ values for magnetite in a Tiva Canyon Tuff sample can extend to 300 mT, which

is the upper limit for prolate spheroids with magnetite-like magnetizations. According to our calculations, $\mu_0 H_{k0}$ for the pigmentary hematite can be much higher, and varies from 1 T to ~10 T in Triassic red chert and from ~1.5 T to > 30 T in Jurassic red chert (Figure 9). As is the case for magnetite, microcoercivity distributions for hematite are nearly symmetric in logarithmic space (Figure 9).

The high coercivity of pigmentary hematite cannot be explained by shape anisotropy (Banerjee, 1971). Özdemir and Dunlop (2014) concluded by studying MD hematite that both magnetoelastic and magnetocrystalline effects contribute to coercivity. However, magnetocrystalline anisotropy causes a gradual coercivity decrease during cooling below room temperature (Liu et al., 2010; Özdemir et al., 2002), which is opposite to the temperature dependence of coercivity observed here. The increasing coercivity trend with cooling in pigmentary hematite is interpreted to be due to magnetoelastic anisotropy, which arises from crystal defects, dislocations, or internal strain (Sunagawa and Flanders, 1965; Sunagawa, 1960; Liu et al., 2010).

5.2. Grain size distribution and unblocking temperature of pigmentary hematite in red chert

Our analysis reveals that both Triassic and Jurassic red chert samples have hematite population with median size of ~75 nm. Additional large amounts of finer hematite < ~35 nm occurs in the Jurassic red chert (Figure 9). The median T_B for each red chert sample is 529 °C (KA1-1B-1), 438 °C (UN2-9B-1), 194 °C (KA6-2L-B-1), and 285 °C (KA6-9B-1). The low unblocking temperatures are also consistent with the small particle size of pigmentary hematite. According to the unblocking temperature and grain size model of Swanson-Hysell et al. (2011, 2019), the median unblocking temperatures in red chert correspond to grain sizes of 100-160 nm, which is within the range of our calculated grain size distributions. The broad unblocking temperature distribution reflects the wide size distribution of natural pigmentary hematite.

We further calculated T_B contours based on the volume and microcoercivity distributions obtained here (Figure 10). Almost the entire pigmentary hematite population in the Triassic red cherts is in the SSD state at room temperature, with unblocking temperatures generally above 300 K (Figure 10a, b). For the Jurassic red cherts, a significant part of the hematite is in the SP state with

unblocking temperatures extending below 100 K. The SP/SSD threshold size for stoner-wohlfarth hematite has been estimated at 25-30 nm (Banerjee, 1971; Özdemir & Dunlop, 2014) and at 17 nm for Al-hematite (Jiang et al., 2014). From our T_B calculations, the SP/SSD threshold size for stoichiometric hematite in the Jurassic red cherts is 7-18 nm, which is close to estimates for Al-hematites.

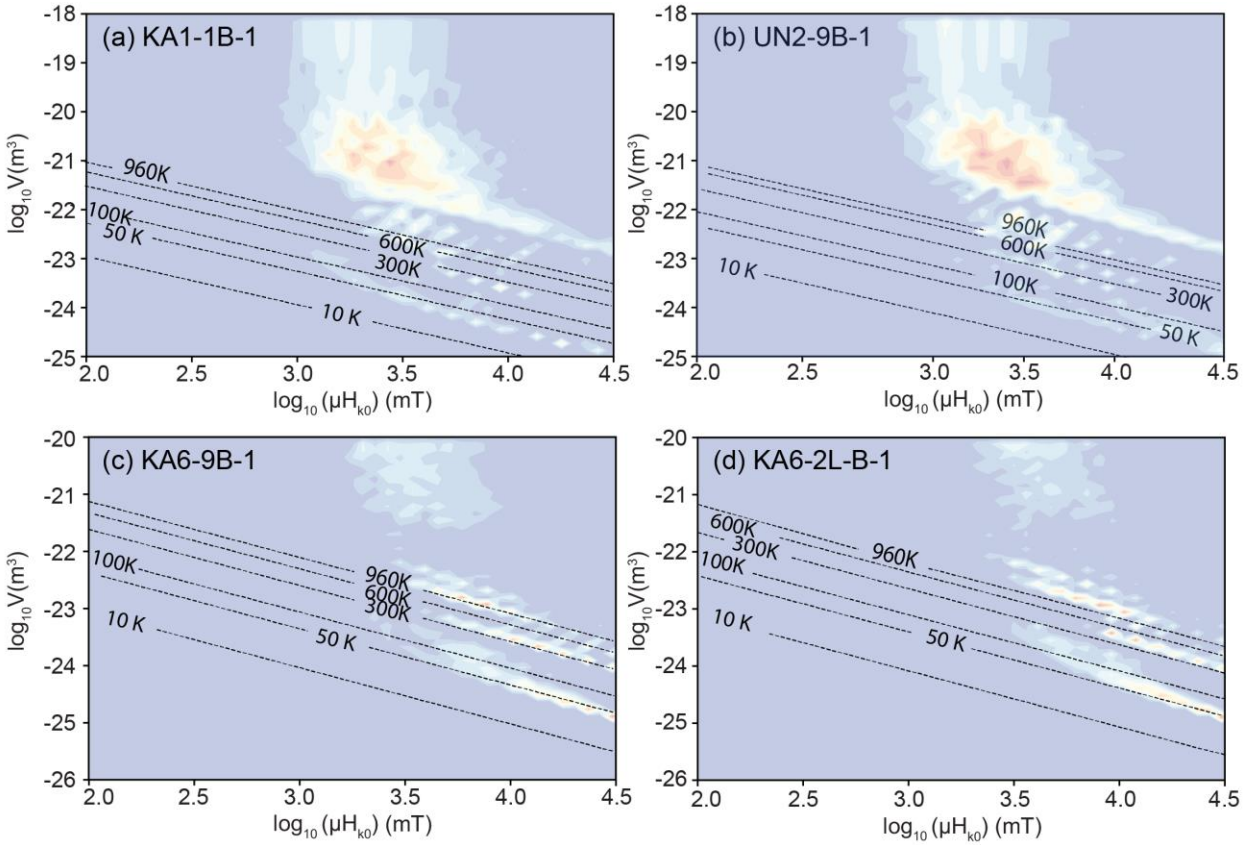

Figure 10 Calculated blocking temperature contours from 10 K to 960 K with f (V, H_{k0}) distributions for (a, b) Triassic and (c, d) Jurassic samples.

Detailed paleomagnetic studies have been conducted on the Inuyama red chert, with four remanence components identified from stepwise thermal demagnetization (Oda and Suzuki, 2000; Shibuya and Sasajima, 1986). The four components are labeled A (70-200 °C), B (200-350 °C), C (350-530 °C), and D (530-680 °C). Components B and C were thought to be Late Cretaceous remagnetizations, although the remagnetization mechanism has been debated. Partial thermal demagnetization (ThD) after alternating field (AF) demagnetization at 80 mT reveals the same

four components (Oda and Suzuki, 2000), which indicates that hematite was at least partly responsible for all four components. This is consistent with the wide unblocking temperature range for hematite in our calculations. Paleomagnetic studies of the Inuyama red chert have all suggested that magnetite is the dominant remanence carrier for components A, B, and C and, thus, magnetite carries the remagnetizations. However, pigmentary hematite should also contribute to the remagnetizations due to its low unblocking temperature, especially for Component B. We suggest this because the unblocking temperature range of component B (200-350 °C) and C (350-530 °C) spans the median hematite unblocking temperature range. Meanwhile, little magnetization for component B was lost between 200 and 350 °C in the original ThD experiment (Figure 6a from Oda and Suzuki (2000)), but the magnetization drops significantly after AF demagnetization of 80 mT (Figure 6c in Oda and Suzuki (2000)). According to our analysis on the magnetite remanent coercivity distribution of the Inuyama red chert at room temperature (Figure 3 and Figure 4), an alternating field of 80 mT will demagnetize most of the magnetite, which suggests that the more significant unblocking feature of component B after AF demagnetization is likely due to pigmentary hematite.

5.3. Limitations of the TFT method for reconstructing hematite grain size distributions

There are two main limitations of the TFT technique for hematite. First, it has the same limitation for hematite as it does for magnetite (Jackson et al., 2006). Reconstructed size distributions are elongated toward the upper left and lower right-hand sides of the Néel diagram, along the blocking contour orientation. This elongation can be due to artifacts in the inversion method, the physical model, and the assumption made, as shown by Jackson et al. (2006) and Dunlop (1965). Resolution limits also remain for inversion due to the restricted orientation distribution of integration paths. Areas of marginal resolution are sampled sparsely by subparallel contours, such as within the small V, high H_{k0} region that is stable only at the lowest temperatures. At the same time, given the small numbers of temperatures employed, the resolution of our results is imperfect, and stripes are evident in the f (V, H_{k0}) distribution rather than a smooth continuous distribution (Figure 8c, d). Increasing the number of temperature steps will improve the resolution, but will also be time and helium expensive, especially for multiple specimens.

Second, compared to magnetite, an additional challenge when modeling hematite is the complexity of its anisotropy. An important assumption in our calculation is that we assign $H_{cr} = 0.524H_K$, which is based on Stoner and Wohlfarth (1948) theory for identical randomly oriented uniaxial particles. Harrison et al. (2019) simulated remanence FORC diagrams for particles with uniaxial, cubic, and hexagonal anisotropy. Among these anisotropy types, randomly oriented, non-interacting particles with uniaxial anisotropy have the lowest H_{cr} values, while H_{cr} for cubic and hexagonal anisotropy is approximately 1.05 and 1.8 times larger, respectively. Therefore, multiaxial anisotropy will produce $0.5 < H_{cr}/H_k < 1$. Magnetic minerals with uniaxial, cubic, and hexagonal anisotropy produce distinctive FORC diagram types (e.g., Egli, 2021; Roberts et al., 2021), which provides a useful way to evaluate the dominant anisotropy type before undertaking TFT analyses. Conventional and remanence FORC diagrams for the Inuyama red chert all have a central ridge up to 1.2 T. Although magnetite dominates the FORC signatures, hematite is responsible for central ridges with coercivities > 300 mT. Ridge-type signatures for conventional and remanence FORC diagrams are explained as a manifestation of uniaxial SD magnetic behavior based on simulations (Harrison et al., 2019). However, instead of being shape dominated, as is the case for magnetite, ridge-type FORC signals for hematite nanoparticles reflect stress-induced uniaxial anisotropy that dominates the intrinsic magnetocrystalline anisotropy (Roberts et al., 2021). This magnetostrictive anisotropy associated with uniaxial internal stress controls the coercivity of hematite, which is consistent with the rapid H_{cr} increase at low temperatures (Figure 5) that is usually enhanced in nanoparticles (Muench et al., 1985; Bruzzone and Ingalls, 1983). Therefore, considering the ridge-type signals observed in both conventional and remanence FORC diagrams for the red chert (see Figure 2 and 3 in Hu et al. (2021)) and H_{cr} variation with temperature, we predict that uniaxial anisotropy dominates pigmentary hematite in red chert and adopt $H_{cr}/H_K = 0.524$. Increased H_{cr}/H_K will result in decreased microcoercivity, increased T_B estimates, and slightly decreased grain size estimates. Thus, when considering variations in the dominant anisotropy type, our calculations at least provide an upper limit of microcoercivity and grain size and a lower T_B limit.

6. Conclusions

Reconstructions of particle microcoercivity and volume distributions were performed with the method of Jackson et al. (2006) for SP/SSD hematite assemblages assuming a dominant uniaxial

anisotropy. The median temperature variation of H_{cr} for pigmentary hematite in Triassic/Jurassic red chert over eight temperatures from 300 K to 10 K follows a modified Kneller's law; $H_{cr}(T) = H_{cr0}\left(1 - (\frac{T}{T_B})^{0.24}\right)$. The coercivity of hematite increases more rapidly than for magnetite with decreasing temperature, and coercivity distribution overlap between the two minerals starts to disappear below 100 K. Microcoercivity distributions that are nearly symmetric in logarithmic space vary from 1 T to ~10 T in Triassic red chert and from ~3 T to 30 T in Jurassic red chert. Both Triassic and Jurassic red chert have wide hematite grain size distributions. Most of the Triassic hematite ranges between ~35 nm to ~160 nm in diameter while the Jurassic red chert has a coaser hematite particles fraction similar to the Triassic hematite and a finer hematite fraction with grain size from a few nanometers to ~35 nm in diameter. Calculated median T_B varies from ~194 °C to 529 °C for red chert samples and T_B contours indicate that most of the Triassic hematite is in the SSD state with a significant SP particle content with T_B < 300 K. The SP/SSD threshold size for pigmentary hematite in Jurassic red chert is estimated to be 8-18 nm. Considering the low and broad T_B distribution in the Inuyama red chert, we propose that pigmentary hematite has a significant contribution to a secondary early Cenozoic thermoviscous magnetization rather than magnetite (Component B defined by Oda and Suzuki (2000)).

Our work demonstrates that the main features of SP/SSD hematite f (V, H_{k0}) distributions can be recovered using the TFT technique, although details should be interpreted judiciously. Smearing of results due to low measurement resolution, artifacts, and variations in dominant anisotropy of hematite should be considered on a case-by-case basis. Ridge-like FORC signatures for red chert are interpreted here to indicate a dominant uniaxial anisotropy. If multiaxial anisotropy is instead dominant in hematite samples (e.g., Roberts et al., 2021), this would increase T_B estimates and decrease microcoercivity and grain size estimates.

Data Availability Statement

All low-temperature magnetic data used here will be uploaded to the Magnetic Information Consortium rock magnetic portal (MagIC; www.earthref.org).

Acknowledgments

We thank Mike Jackson for providing the original TFT code. This work was supported by the National Institute of Advanced Industrial Science and Technology, Ministry of Economy, Trade and Industry, Japan, and the Australian Research Council through grants DP160100805 and DP200100765.

Appendix A

Bayesian regression was performed using the PyMC3 Python package (Salvatier et al., 2016). The parameterizations of the Bayesian prior distributions for H_{cr0}, T_B, α and fitting error σ are provided below.

1. H_{cr0}

The prior for $\mu_0 H_{cr0}$ follows a log normal distribution with median value of 0 and variance of 1. Thus, the probability density function can be expressed as:

$$p(\mu_0 H_{cr0}) = \frac{1}{\mu_0 H_{cr0}\sqrt{2\pi}} \exp\left(-\frac{\ln(\mu_0 H_{cr0})^2}{2}\right) \quad (A1)$$

2. T_B

Theoretically, T_B can vary between 0 and 960 K for hematite. For better calculation efficiency, we set all variable values between 0 and 1 in the Bayesian regression. Therefore, instead of T_B, we use $T_B/1000$ to follow a Beta distribution with $\alpha = 2$ and $\beta = 2$, the probability density function can be expressed as:

$$p\left(\frac{T_B}{1000}\right) = \frac{\frac{T_B}{1000} \times \left(1 - \frac{T_B}{1000}\right)}{B(2,2)}; \text{ and} \quad (A2)$$

$$B(2,2) = \frac{\Gamma(2)\Gamma(2)}{\Gamma(4)} \quad (A3)$$

Where Γ is the Gamma function.

3. α and n

α and n follow a Beta distribution with α = 8 and β = 8, the probability density function can be expressed as:

$$p(\alpha) = \frac{\alpha^7 \times (1-\alpha)^7}{B(8,8)} \text{ or } p\left(\frac{n}{50}\right) = \frac{\left(\frac{n}{50}\right)^7 \times \left(1-\left(\frac{n}{50}\right)\right)^7}{B(8,8)}, \text{with} \quad (A4, A5)$$

$$B(8,8) = \frac{\Gamma(8)\Gamma(8)}{\Gamma(16)} \quad (A6)$$

Based on previous studies, n rarely exceeds the value of 50. Therefore, we normalized n by 50 for it to vary from 0 to 1. Γ in equation (A6) is the Gamma function.

4. Fitting error σ

σ follows a half-Cauchy distribution with location parameter of 0 and scale parameter of 1. The probability density function can be expressed as:

$$f(\sigma, 1) = \frac{2}{\pi(1+\sigma)} \quad (A7)$$

The, no U-Turn Sampler (NUTS) from the Python Pymc3 package was used for sampling, in where we set both the sampling number and iteration number to 4000.

Statistical results of Bayesian regression using equation (3) and equation (4), respectively are listed. Two hundreds regression curves for each sample are shown in Figure 5. In the following tables, hdi_3% and hdi_97% are the lower and upper bounds of the 97% high density interval. R_hat is the Gelman-Rubin convergence statistic, where a value of 1 indicates that the chains have converged.

Table A1 Posterior statistics of Bayesian regression of equation (3)

	Median	Standard deviation	hdi_3%[1]	hdi_97%[2]	R_hat[3]
n	28.650	3.700	21.650	35.600	1
$\mu_0 H_{cr0}$ (T) (KA1-1B-1)	1.402	0.137	1.133	1.649	1
$\mu_0 H_{cr0}$ (T) (UN2-9B-1)	1.424	0.139	1.166	1.682	1
$\mu_0 H_{cr0}$ (T) (KA6-9B-1)	1.581	0.145	1.308	1.853	1
$\mu_0 H_{cr0}$ (T) (KA6-2L-B-1)	1.645	0.145	1.371	1.916	1
σ	0.253	0.037	0.189	0.321	1

Table A2 Posterior statistics of Bayesian regression of equation (4)

	mean	Standard deviation	hdi_3%[1]	hdi_97%[2]	R_hat[3]
α	0.240	0.052	0.151	0.339	1
$\mu_0 H_{cr0}$ (T) (KA1-1B-1)	2.500	0.383	1.829	3.211	1
$\mu_0 H_{cr0}$ (T) (UN2-9B-1)	2.667	0.405	1.947	3.446	1
$\mu_0 H_{cr0}$ (T) (KA6-9B-1)	3.246	0.494	2.335	4.164	1
$\mu_0 H_{cr0}$ (T) (KA6-2L-B-1)	3.648	0.561	2.627	4.664	1
T_B/100 (K) (KA1-1B-1)	0.803	0.099	0.621	0.972	1
T_B/1000 (K) (UN2-9B-1)	0.717	0.103	0.534	0.919	1
T_B/1000 (K) (KA6-9B-1)	0.558	0.076	0.425	0.701	1
T_B/1000 (K) (KA6-2L-B-1)	0.467	0.054	0.370	0.567	1
σ	0.111	0.019	0.078	0.148	1

[1] hdi_3% represents the lower bounds of the 97% high density interval of the corresponding posterior distribution.
[2] hdi_97% represents the upper bounds of the 97% high density interval of the corresponding posterior distribution
[3] R_hat is the Gelman-Rubin convergence statistic, which estimates the degree of convergence of a random Markov Chain. Values close to one indicate convergence to the underlying distribution.

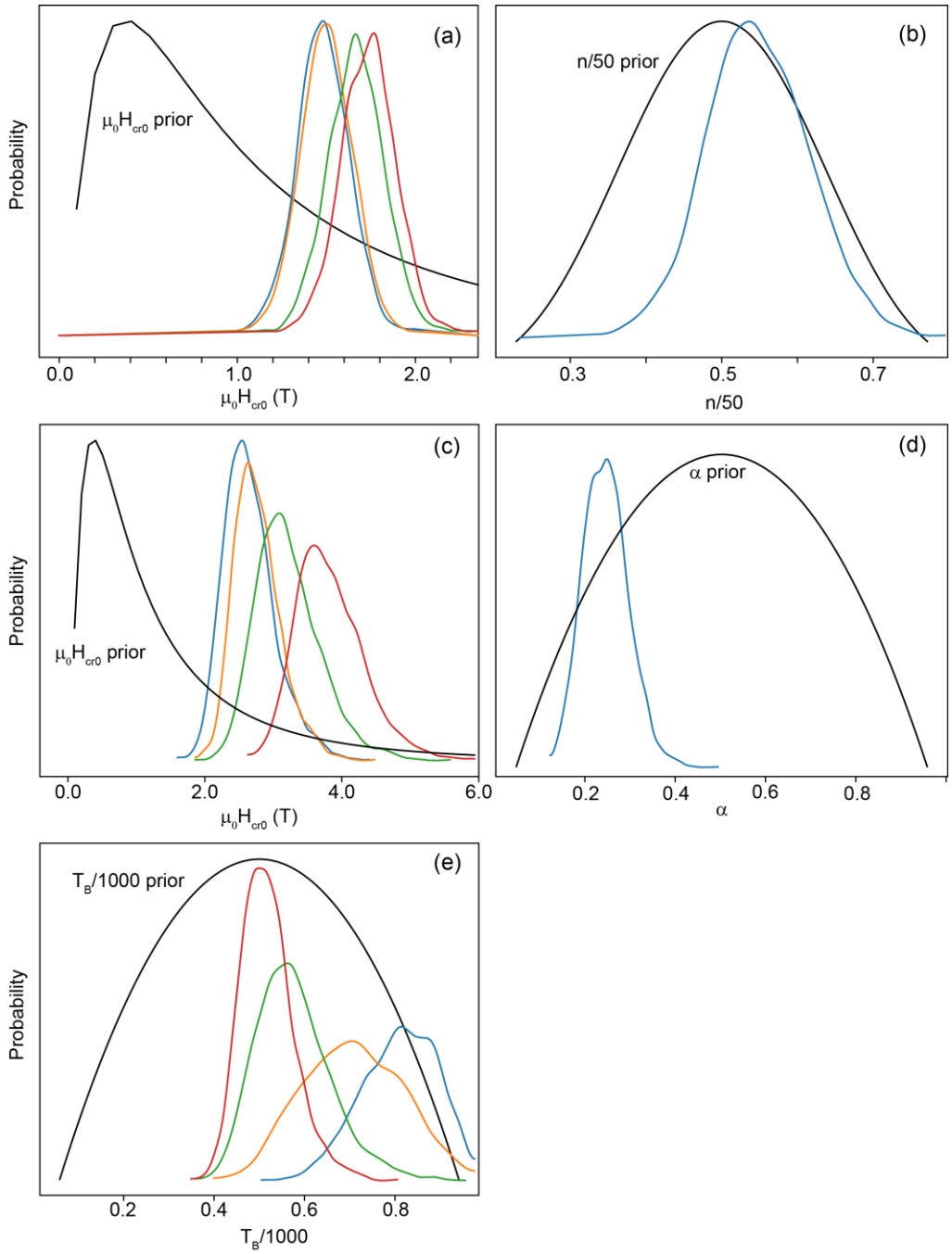

Figure A1 The prior distribution (black lines) and posterior distribution (colored lines) of parameters in the Bayesian model for (a-b) equation (3) and (c-e) equation (4). Blue, orange, green, and red lines represent corresponding parameters for sample KA1-1B-1, UN2-9B-1, KA6-9B-1 and KA6-2L-B-1, respectively.

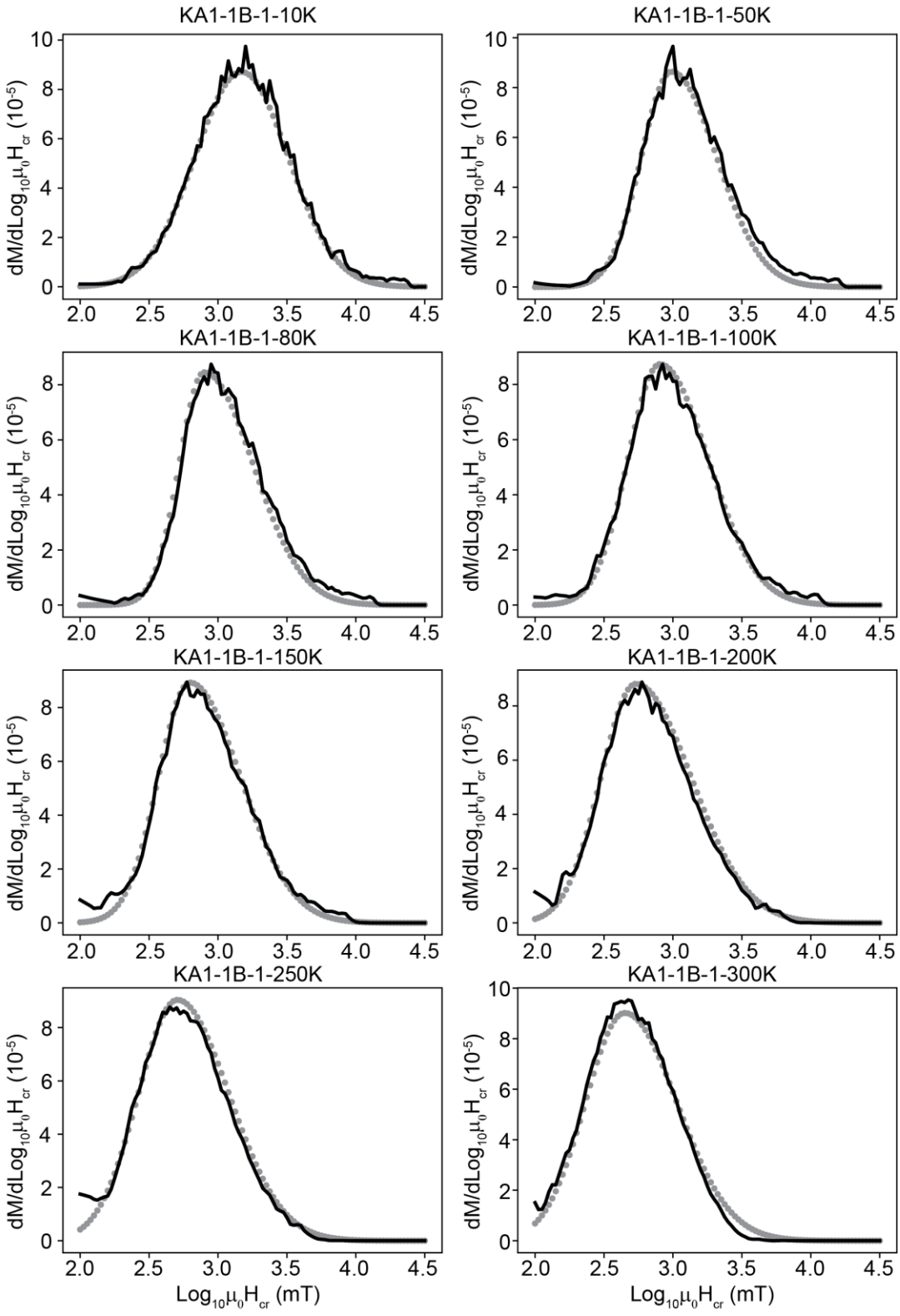

Figure A2 Reconstructed (black solid lines) and measured backfield remanence curve derivatives (gray dots) for Triassic sample KA1-1B-1.

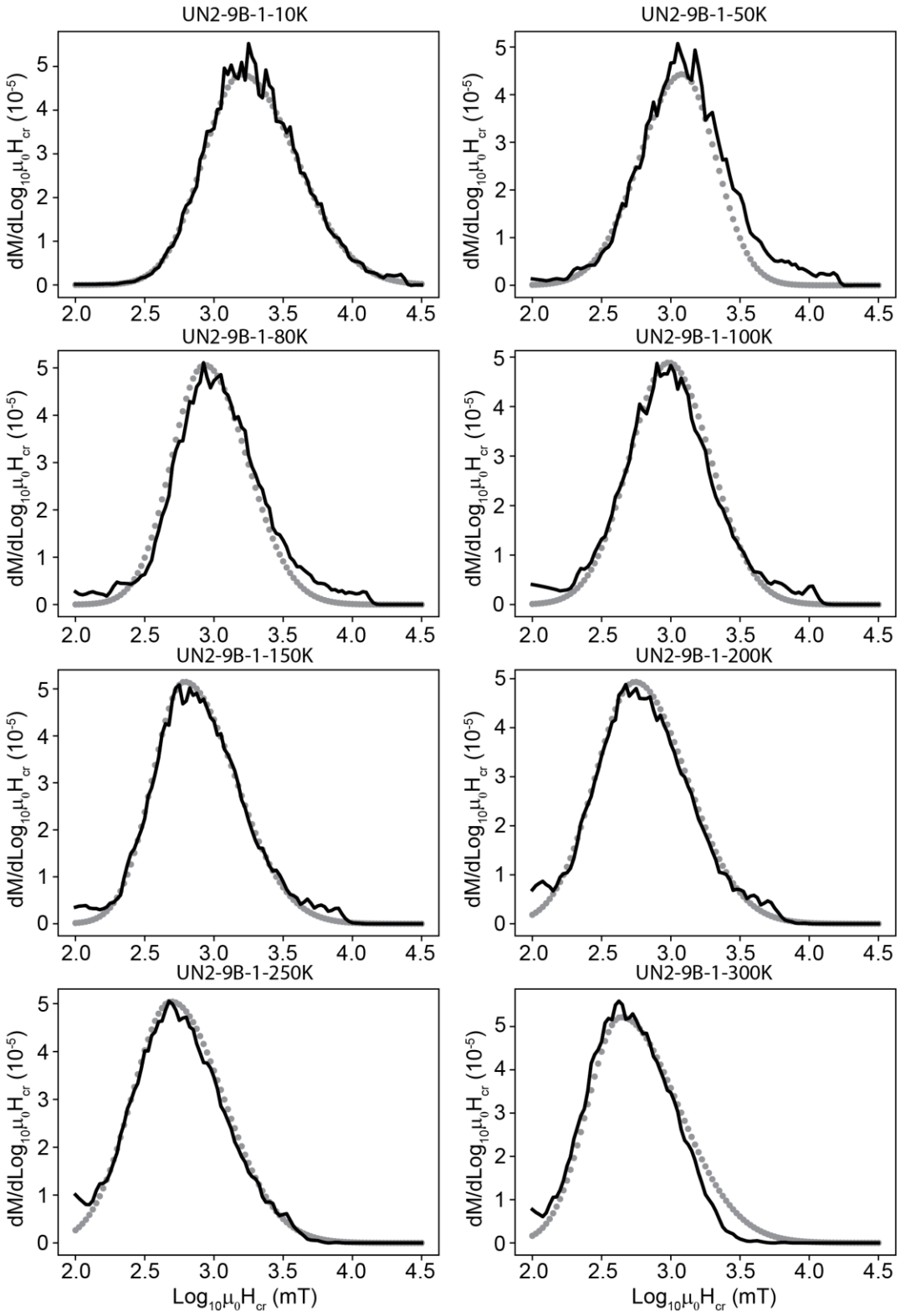

Figure A3 Reconstructed (black solid lines) and measured backfield remanence curve derivatives (gray dots) for Triassic sample UN2-9B-1.

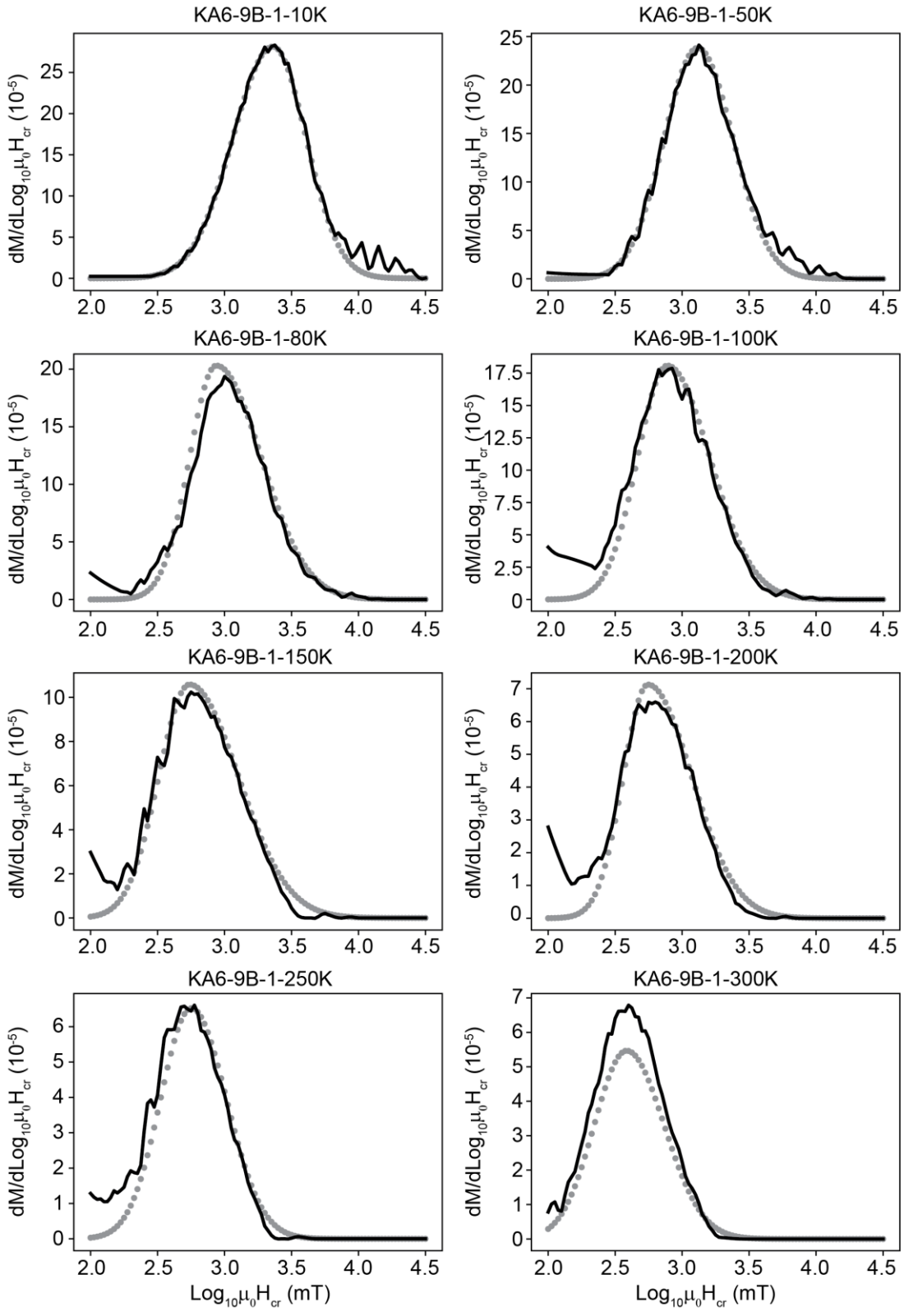

Figure A4 Reconstructed (black solid lines) and measured backfield remanence curve derivatives (gray dots) for Jurassic sample KA6-9B-1.

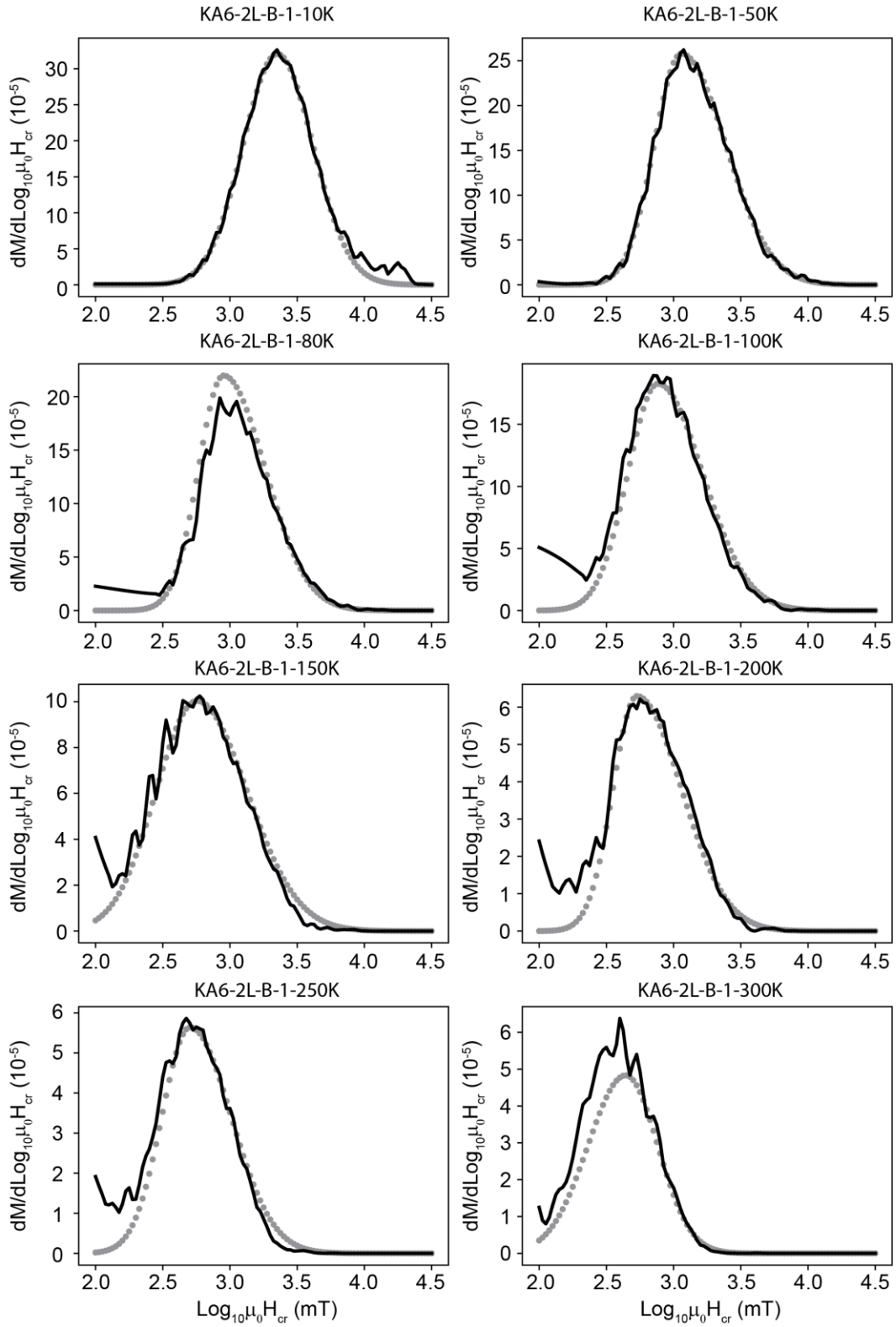

Figure A5 Reconstructed (black solid lines) and measured backfield remanence curve derivatives (gray dots) for Jurassic sample KA6-2L-B-1.

References

Abrajevitch, A., R. S. Hori, & K. Kodama (2011), Magnetization carriers and remagnetization of bedded chert, *Earth and Planetary Science Letters*, *305*(1-2), 135-142.

Abrajevitch, A., R. S. Hori, & K. Kodama (2013), Rock magnetic record of the Triassic-Jurassic transition in pelagic bedded chert of the Inuyama section, Japan, *Geology*, *41*(7), 803-806.

Abrajevitch, A., B. J. Pillans, A. P. Roberts, & K. Kodama (2018), Magnetic properties and paleomagnetism of zebra rock, western Australia: Chemical remanence acquisition in hematite pigment and ediacaran geomagnetic field behavior, *Geochemistry Geophysics Geosystems*, *19*(3), 732-748.

Banerjee, S. K. (1963), An attempt to observe basal plane anisotropy of hematite, *Philosophical Magazine*, *8*(96), 2119-2120, doi:10.1080/14786436308209106.

Banerjee, S. K. (1971), New grain size limits for palaeomagnetic stability in haematite, *Nature-Physical Science*, *232*(27), 15-&, doi:10.1038/physci232015a0.

Beck, M. E., R. F. Burmester, & B. A. Housen (2003), The red bed controversy revisited: shape analysis of Colorado Plateau units suggests long magnetization times, *Tectonophysics*, *362*(1), 335-344, doi:10.1016/S0040-1951(02)00644-3.

Bilardello, D., & K. P. Kodama (2010a), Palaeomagnetism and magnetic anisotropy of Carboniferous red beds from the Maritime Provinces of Canada: evidence for shallow palaeomagnetic inclinations and implications for North American apparent polar wander, *Geophysical Journal International*, *180*(3), 1013-1029, doi:10.1111/j.1365-246X.2009.04457.x.

Bilardello, D., & K. P. Kodama (2010b), Rock magnetic evidence for inclination shallowing in the early Carboniferous Deer Lake Group red beds of western Newfoundland, *Geophysical Journal International*, *181*(1), 275-289, doi:10.1111/j.1365-246X.2010.04537.x.

Bloch, F. (1930), Zur Theorie des Ferromagnetismus, *Zeitschrift für Physik*, 61(3), 206-219, doi:10.1007/BF01339661.

Bruzzone, C. L., & R. Ingalls (1983), Mossbauer-effect study of the morin transition and atomic positions in hematite under pressure, *Physical Review B*, *28*(5), 2430-2440, doi:10.1103/PhysRevB.28.2430.

Butler, R. (1992), *Paleomagnetism: Magnetic domains to geologic terranes*, Blackwell Scientific Publications, Boston.

Collinson, D. W. (1969), Investigations into stable remanent magnetization of sediments, *Geophysical Journal of the Royal Astronomical Society*, *18*(2), 211-222, doi:10.1111/j.1365-246X.1969.tb03563.x.

Cornell, R. M., & U. Schwertmann (2004), *The Iron Oxides: Structure, Properties, Reactions, Occurences and Uses*, 664 pp., Wiley-VCH Verlag GmbH & Co. KGaA, doi:10.1002/3527602097.

Dekkers, M. J. (1990), Magnetic-properties of natural goethite. 3. Magnetic-behavior and properties of minerals originating from goethite dehydration during thermal demagnetization, *Geophysical Journal International*, *103*(1), 233-250, doi:10.1111/j.1365-246X.1990.tb01765.x.

Dunlop, D. J. (1965), Grain distributions in rocks containing single domain grains, *Journal of Geomagnetism and Geoelectricity*, *17*(3-4), 459-&, doi:10.5636/jgg.17.459.

Dunlop, D. J., & Ö. Özdemir (2000), Effect of grain size and domain state on thermal demagnetization tails, *Geophysical Research Letters*, *27*(9), 1311-1314, doi: 10.1029/1999GL008461.

Dunlop, D. J., Ö. Özdemir, D. A. Clark, & P. W. Schmidt (2000), Time–temperature relations for the remagnetization of pyrrhotite (Fe_7S_8) and their use in estimating paleotemperatures, *Earth and Planetary Science Letters*, *176*(1), 107-116, doi:10.1016/S0012-821X(99)00309-X.

Egglseder, M. S., A. R. Cruden, A. G. Tomkins, S. A. Wilson, & A. D. Langendam (2018), Colloidal origin of microbands in banded iron formations, *Geochemical Perspectives Letters*, *6*, 43-49, doi:10.7185/geochemlet.1808.

Egli, R. (2021), Magnetic Characterization of Geologic Materials with First-Order Reversal Curves, in *Magnetic Measurement Techniques for Materials Characterization*, edited by V. Franco and B. Dodrill, pp. 455-604, Springer International Publishing, Cham, doi:10.1007/978-3-030-70443-8_17.

Egli, R., A. P. Chen, M. Winklhofer, K. P. Kodama, & C.-S. Horng (2010), Detection of noninteracting single domain particles using first-order reversal curve diagrams, *Geochemistry, Geophysics, Geosystems*, *11*(1), doi:10.1029/2009gc002916.

Frank, U., & N. R. Nowaczyk (2008), Mineral magnetic properties of artificial samples systematically mixed from haematite and magnetite, *Geophysical Journal International*, *175*(2), 449-461.

Guyodo, Y., A. Mostrom, R. L. Penn, & S. K. Banerjee (2003), From nanodots to nanorods: oriented aggregation and magnetic evolution of nanocrystalline goethite, *Geophysical Research Letters*, *30*(10), doi:10.1029/2003gl017021.

Harrison, R. J., X. Zhao, P. Hu, T. Sato, D. Heslop, A. R. Muxworthy, H. Oda, V. S. C. Kuppili, & A. P. Roberts (2019), Simulation of remanent, transient, and induced FORC diagrams for interacting particles with uniaxial, cubic, and hexagonal anisotropy, *Journal of Geophysical Research: Solid Earth*, *124*(12), 12404-12429, doi:10.1029/2019JB018050.

Hendriksen, P. V., S. Linderoth, & P. A. Lindgard (1993), Finite-size modifications of the magnetic-properties of clusters, *Physical Review B*, *48*(10), 7259-7273, doi:10.1103/PhysRevB.48.7259.

Hu, P. X., H. Oda, X. Zhao, R. J. Harrison, D. Heslop, T. Sato, A. R. Muxworthy, & A. P. Roberts (2021), Assessment of magnetic techniques for understanding complex mixtures of magnetite and hematite: The Inuyama red chert, *Journal of Geophysical Research-Solid Earth*, *126*(1), doi:10.1029/2020JB019518.

Huang, W., M. J. Jackson, M. J. Dekkers, P. Solheid, B. Zhang, Z. Guo, & L. Ding (2019), Nanogoethite as a potential indicator of remagnetization in red beds, *Geophysical Research Letters*, *46*(22), 12841-12850, doi:10.1029/2019GL084715.

Hyodo, M., T. Sano, M. Matsumoto, Y. Seto, B. Bradák, K. Suzuki, J.-i. Fukuda, M. Shi, & T. Yang (2020), Nanosized authigenic magnetite and hematite particles in mature-paleosol phyllosilicates: New evidence for a magnetic enhancement mechanism in loess sequences of China, *Journal of Geophysical Research: Solid Earth*, *125*(3), e2019JB018705, doi:10.1029/2019JB018705.

Jackson, M., B. Carter-Stiglitz, R. Egli, & P. Solheid (2006), Characterizing the superparamagnetic grain distribution f(V, Hk) by thermal fluctuation tomography, *Journal of Geophysical Research: Solid Earth*, *111*(B12), doi:10.1029/2006jb004514.

Jacobsen, H. (2014), *Magnetic properties of nano-scale hematite: theory, experiments and simulations*, University of Copenhagen.

Jiang, Z., Q. Liu, A. P. Roberts, M. J. Dekkers, V. Barrón, J. Torrent, & S. Li (2022), The magnetic and color reflectance properties of hematite: from Earth to Mars, *Reviews of Geophysics*, *60*(1), e2020RG000698, doi:10.1029/2020RG000698.

Jiang, Z. X., Q. S. Liu, M. J. Dekkers, V. Barron, J. Torrent, & A. P. Roberts (2016), Control of Earth-like magnetic fields on the transformation of ferrihydrite to hematite and goethite, *Scientific Reports*, *6*, doi:10.1038/srep30395.

Jiang, Z. X., Q. S. Liu, M. J. Dekkers, C. Colombo, Y. J. Yu, V. Barron, & J. Torrent (2014), Ferro and antiferromagnetism of ultrafine-grained hematite, *Geochemistry Geophysics Geosystems*, *15*(6), 2699-2712, doi:10.1002/2014gc005377.

Jiang, Z. X., Q. S. Liu, M. J. Dekkers, X. Zhao, A. P. Roberts, Z. Y. Yang, C. S. Jin, & J. X. Liu (2017), Remagnetization mechanisms in Triassic red beds from South China, *Earth and Planetary Science Letters*, *479*, 219-230.

Jones, D. L., & B. Murchey (1986), Geologic significance of paleozoic and mesozoic radiolarian chert, *Annual Review of Earth and Planetary Sciences*, *14*, 455-492.

Kletetschka, G., & P. J. Wasilewski (2002), Grain size limit for SD hematite, *Physics of the Earth and Planetary Interiors*, 129(1), 173-179, doi: 10.1016/S0031-9201(01)00271-0.

Kneller, E. F., & F. E. Luborsky (1963), Particle size dependence of coercivity and remanence of single-domain particles, *Journal of Applied Physics*, *34*(3), 656-658, doi:10.1063/1.1729324.

Lagroix, F., & Y. Guyodo (2017), A new tool for separating the magnetic mineralogy of complex mineral assemblages from low temperature magnetic behavior, *Frontiers in Earth Science*, *5*(61), doi:10.3389/feart.2017.00061.

Larrasoaña, J. C., A. P. Roberts, E. J. Rohling, M. Winklhofer, & R. Wehausen (2003), Three million years of monsoon variability over the northern Sahara, *Climate Dynamics*, 21(7), 689-698, doi:10.1007/s00382-003-0355-z.

Lepre, C. J., & P. E. Olsen (2021), Hematite reconstruction of Late Triassic hydroclimate over the Colorado Plateau, *Proceedings of the National Academy of Sciences*, *118*(7), e2004343118, doi:10.1073/pnas.2004343118.

Liu, Q., V. Barrón, J. Torrent, H. Qin, & Y. Yu (2010), The magnetism of micro-sized hematite explained, *Physics of the Earth and Planetary Interiors*, *183*(3), 387-397, doi:10.1016/j.pepi.2010.08.008.

Liu, Q. S., J. Bloemendal, J. Torrent, & C. L. Deng (2006), Contrasting behavior of hematite and goethite within paleosol S5 of the Luochuan profile, Chinese Loess Plateau, *Geophysical Research Letters*, 33(20), doi:10.1029/2006gl027172.

Maaz, K., A. Mumtaz, S. K. Hasanain, & M. F. Bertino (2010), Temperature dependent coercivity and magnetization of nickel ferrite nanoparticles, Journal of Magnetism and Magnetic Materials, 322(15), 2199-2202, doi:10.1016/j.jmmm.2010.02.010.

Martin-Hernandez, F., & S. Guerrero-Suárez (2012), Magnetic anisotropy of hematite natural crystals: high field experiments, *International Journal of Earth Sciences*, *101*(3), 637-647, doi:10.1007/s00531-011-0665-z.

Martinez, B., A. Roig, X. Obradors, E. Molins, A. Rouanet, & C. Monty (1996), Magnetic properties of gamma-Fe_2O_3 nanoparticles obtained by vaporization condensation in a solar furnace, *Journal of Applied Physics*, *79*(5), 2580-2586, doi:10.1063/1.361125.

Matsuo, M., K. Kubo, & Y. Isozaki (2003), Moessbauer spectroscopic study on characterization of iron in the Permian to Triassic deep-sea chert from Japan, *Hyperfine Interactions*, *5*, 435-438.

Maxbauer, D. P., J. M. Feinberg, & D. L. Fox (2016), MAX UnMix: A web application for unmixing magnetic coercivity distributions, *Computers & Geosciences*, *95*, 140-145, doi: 10.1016/j.cageo.2016.07.009.

Menyeh, A., & W. O'Reilly (1995), The coercive force of fine particles of monoclinic pyrrhotite (Fe_7S_8) studied at elevated temperature, *Physics of the Earth and Planetary Interiors*, *89*(1), 51-62, doi: 10.1016/0031-9201(94)02999-R.

Muench, G. J., S. Arajs, & E. Matijevic (1985), The Morin transition in small Alpha-Fe_2O_3 particles, *Physica Status Solidi a-Applied Research*, *92*(1), 187-192, doi:DOI 10.1002/pssa.2210920117.

Néel, L. (1949), Théorie du traînage magnétique des ferromagnétiques en grains fins avec application aux terres cuites, *Annales de Geophysique*, *5*, 99--136.

Oda, H., & H. Suzuki (2000), Paleomagnetism of Triassic and Jurassic red bedded chert of the Inuyama area, central Japan, *Journal of Geophysical Research-Solid Earth*, *105*(B11), 25743-25767.

Özdemir, O., & D. J. Dunlop (2014), Hysteresis and coercivity of hematite, *Journal of Geophysical Research-Solid Earth*, *119*(4), 2582-2594, doi:10.1002/2013jb010739.

Özdemir, Ö., & D. J. Dunlop (2002), Thermoremanence and stable memory of single-domain hematites, *Geophysical Research Letters*, *29*(18), 24-21-24-24, doi: 10.1029/2002GL015597.

Peters, C., & M. J. Dekkers (2003), Selected room temperature magnetic parameters as a function of mineralogy, concentration and grain size, *Physics and Chemistry of the Earth, Parts A/B/C*, *28*(16), 659-667, doi:10.1016/S1474-7065(03)00120-7.

Roberts, A. P., X. Zhao, D. Heslop, A. Abrajevitch, Y.H. Chen, P. Hu, Z. Jiang, Q. Liu, & B. J. Pillans (2020), Hematite (α-Fe2O3) quantification in sedimentary magnetism: limitations of existing proxies and ways forward, *Geoscience Letters*, *7*(1), 8, doi:10.1186/s40562-020-00157-5.

Roberts, A. P., X. Zhao, P. Hu, A. Abrajevitch, Y. Chen, R. Harrison, D. Heslop, Z. Jiang, J. Li, Q. Liu, A. R. Muxworthy, H. Oda, H. St. C. O'Neill, B. J. Pillans & T. Sato (2021), Magnetic domain state and anisotropy in hematite (α-Fe_2O_3) from first-order reversal curve diagrams, *Journal of Geophysical Research: Solid Earth*, *126*(12), e2021JB023027, doi:10.1029/2021JB023027.

Salvatier, J., T. V. Wiecki, & C. Fonnesbeck (2016), Probabilistic programming in Python using PyMC3, Peerj Computer Science, doi:ARTNe5510.7717/peerj-cs.55.

Satheesh, M., A. R. Paloly, C. K. Krishna Sagar, K. G. Suresh, & M. J. Bushiri (2018), Improved coercivity of solvothermally grown hematite (α-Fe_2O_3) and hematite/graphene oxide nanocomposites (α-Fe_2O_3/GO) at low temperature, *physica status solidi (a)*, *215*(2), 1700705, doi:10.1002/pssa.201700705.

902 Schwertmann, U. (1991), Solubility and dissolution of iron-oxides, *Plant and Soil*, *130*(1-2), 1-25, doi:
903 10.1007/Bf00011851.
904 Shibuya, H., & S. Sasajima (1986), Paleomagnetism of red cherts - a case-study in the Inuyama area, central
905 Japan, *Journal of Geophysical Research-Solid Earth and Planets*, *91*(B14), 14105-14116.
906 Stoner, E. C., & E. P. Wohlfarth (1948), A mechanism of magnetic hysteresis in heterogeneous alloys,
907 Philosophical Transactions of the Royal Society of London. Series A, *Mathematical and Physical*
908 *Sciences*, 240(826), 599-642, doi:10.1098/rsta.1948.0007.
909 Sun, S., K. O. Konhauser, A. Kappler, & Y.L. Li (2015), Primary hematite in Neoarchean to
910 Paleoproterozoic oceans, *GSA Bulletin*, *127*(5-6), 850-861, doi:10.1130/b31122.1.
911 Sunagawa, I. (1960), Growth history of hematite, *American Mineralogist*, *45*(5-6), 566-575.
912 Sunagawa, I., & P. J. Flanders (1965), Structural and magnetic studies in hematite single crystals,
913 *Philosophical Magazine*, *11*(112), 747-&, doi:10.1080/14786436508230080.
914 Swanson-Hysell, N. L., L. M. Fairchild, & S. P. Slotznick (2019), Primary and secondary red bed
915 magnetization constrained by fluvial intraclasts, *Journal of Geophysical Research: Solid Earth*, *124*(5),
916 4276-4289, doi:10.1029/2018jb017067.
917 Swanson-Hysell, N. L., J. M. Feinberg, T. S. Berquo, & A. C. Maloof (2011), Self-reversed magnetization
918 held by martite in basalt flows from the 1.1-billion-year-old Keweenawan rift, Canada, *Earth and*
919 *Planetary Science Letters*, *305*(1-2), 171-184.
920 Tauxe, L., D. V. Kent, & N. D. Opdyke (1980), Magnetic components contributing to the NRM of middle
921 Siwalik red beds, *Earth and Planetary Science Letters*, *47*(2), 279-284, doi:10.1016/0012-
922 821x(80)90044-8.
923 Van Der Voo, R., & T. H. Torsvik (2012), The history of remagnetization of sedimentary rocks: Deceptions,
924 developments and discoveries, *371*(1), 23-53.
925 Zhang, D. J., K. J. Klabunde, C. M. Sorensen, & G. C. Hadjipanayis (1998), Magnetization temperature
926 dependence in iron nanoparticles, *Physical Review B*, *58*(21), 14167-14170,
927 doi:10.1103/PhysRevB.58.14167.

928